AD-A137 153 FLUORESCENCE AND ELECTRON ENERGY LOSS CROSS SECTIONS IN 1/1
MERCURIC BROMIDE..(U) WESTINGHOUSE RESEARCH AND
DEVELOPMENT CENTER PITTSBURGH PA P J CHANTRY ET AL.
UNCLASSIFIED 22 DEC 83 83-9C1-ELOSS-R1 N00014-83-C-0240 F/G 7/4 NL

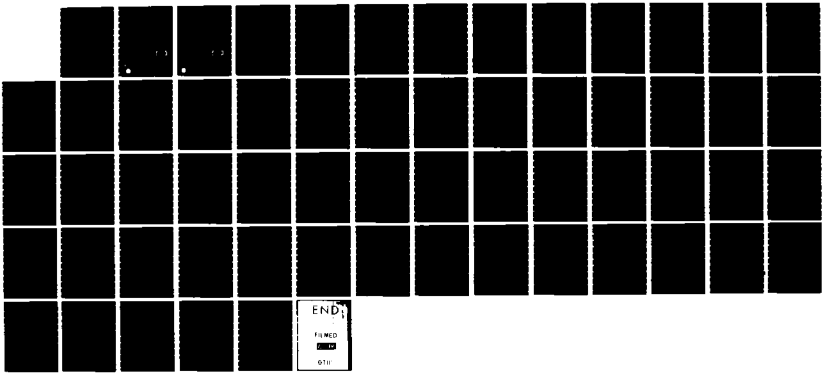

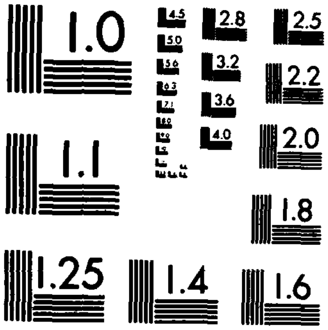

MICROCOPY RESOLUTION TEST CHART
NATIONAL BUREAU OF STANDARDS-1963-A

FLUORESCENCE AND ELECTRON ENERGY LOSS CROSS SECTIONS IN MERCURIC BROMIDE

12

P. J. Chantry and C. L. Chen

FINAL REPORT

For Period of March 17, 1983 to October 31, 1983

Contract No. N00014-83-C-0240

Sponsored by
Office of Naval Research

Monitored by
Office of Naval Research

December 22, 1983

DISTRIBUTION STATEMENT A
Approved for public release
Distribution Unlimited

Westinghouse R&D Center
1310 Beulah Road
Pittsburgh, Pennsylvania 15235

FLUORESCENCE AND ELECTRON ENERGY LOSS CROSS SECTIONS IN MERCURIC BROMIDE

P. J. Chantry and C. L. Chen

FINAL REPORT

For Period of March 17, 1983 to October 31, 1983

Contract No. N00014-83-C-0240

Sponsored by
Office of Naval Research

Monitored by
Office of Naval Research

December 22, 1983

Westinghouse R&D Center
1310 Beulah Road
Pittsburgh, Pennsylvania 15235

SECURITY CLASSIFICATION OF THIS PAGE *(When Data Entered)*

REPORT DOCUMENTATION PAGE

READ INSTRUCTIONS BEFORE COMPLETING FORM

1. REPORT NUMBER
83-9C1-ELOSS-R1

2. GOVT ACCESSION NO.
AD-A137 153

3. RECIPIENT'S CATALOG NUMBER

4. TITLE *(and Subtitle)*
Fluorescence and Electron Energy Loss Cross Sections in Mercuric Bromide

5. TYPE OF REPORT & PERIOD COVERED
Final Report
3/17/83 - 10/31/83

6. PERFORMING ORG. REPORT NUMBER

7. AUTHOR(s)
P. J. Chantry and C. L. Chen

8. CONTRACT OR GRANT NUMBER(s)
N00014-83-C-0240

9. PERFORMING ORGANIZATION NAME AND ADDRESS
Westinghouse R&D Center
1310 Beulah Road
Pittsburgh, PA 15235

10. PROGRAM ELEMENT, PROJECT, TASK AREA & WORK UNIT NUMBERS

11. CONTROLLING OFFICE NAME AND ADDRESS
Office of Naval Research
800 North Quincy Street
Arlington, VA 22217

12. REPORT DATE
Dec. 22, 1983

13. NUMBER OF PAGES
55

14. MONITORING AGENCY NAME & ADDRESS *(if different from Controlling Office)*

15. SECURITY CLASS. *(of this report)*
Unclassified

15a. DECLASSIFICATION/DOWNGRADING SCHEDULE

16. DISTRIBUTION STATEMENT *(of this Report)*

Approved for public release; distribution unlimited.

17. DISTRIBUTION STATEMENT *(of the abstract entered in Block 20, if different from Report)*

18. SUPPLEMENTARY NOTES

19. KEY WORDS *(Continue on reverse side if necessary and identify by block number)*

Mercuric Bromide, Dissociation, Emission, Fluorescence, Cross Sections, Electron, Impact, Beams, Laser, Excitation, Threshold, Collisions.

20. ABSTRACT *(Continue on reverse side if necessary and identify by block number)*

(see over)

DD FORM 1 JAN 73 1473 EDITION OF 1 NOV 65 IS OBSOLETE
S/N 0102-LF-014-6601

Unclassified
SECURITY CLASSIFICATION OF THIS PAGE *(When Data Entered)*

20.

Abstract

Computer modelling of HgBr discharge lasers requires as input the various cross sections for electron impact on $HgBr_2$. This report describes measurements of the wavelength resolved emission cross section measured between 240 and 530 nm. This range encompasses three bands: The (D-X), (C-X), and B-X which have been documented and discussed previous. In addition we find a fourth band which appears on the long wavelength side of the (C-X) band, and overlaps the short wavelength tail of the (B-X) band. Measurements of the wavelengths at which local maxima appear in the fluorescence agree acceptably with Wielands' data on this band, which we designate as the (B'-X) band. A systematic approach to partitioning the spectrum between the various bands has been adopted in order to derive total band emission cross sections for all four bands. A more extensive series of measurements on the "benchmark" He line emission cross sections has led to a revised method of calibrating the HgBr data. As a result of these changes in the method of interpreting the data our previous measurement of the emission cross section for the (B-X) continuum is revised downwards, from 3.2×10^{-18} cm^2 to 2.25×10^{-18} cm^2 in the plateau region. The thresholds for the (B'-X), (C-X) and (D-X) bands, measured at their peak wavelengths, are 7.45, 7.40 and 7.65 eV respectively. The lumped emission cross section for the D, C and B'-X bands is comparable to the B-X cross section. Trapped electron measurements identify energy loss thresholds at 5.1, 6.0, 7.4 and 9.15 eV, and at approximately 3.7 eV. The relative magnitudes of the trapped electron signals associated with the 6.0 eV and the 7.4 eV processes, when compared with the corresponding emission cross sections, suggest that the 7.4 eV process produces mostly non-radiating products.

CONTENTS

1. SUMMARY

1.1 Objectives and Approach

The general objective of the present program was to provide additional information regarding electron impact energy loss cross sections in $HgBr_2$ to complement other available measured cross sections for this molecule. The latter consisted of the cross sections for negative and positive ion production (Wiegand & Boedecker, 1982) and the cross section for production of the $HgBr^*(B)$ state measured by us previously (Chantry and Chen, 1982). The specific objectives were to (i) measure the shape and magnitude of the cross section for production of the $HgBr^*(C)$ state, i.e.,

$$e + HgBr_2 \rightarrow HgBr^* \; (C^2\pi_{1/2}) + Br + e \qquad (1)$$

and (ii) to measure threshold energies for other inelastic energy loss processes.

The same approach is used to measure the cross section for reaction (1) as was adopted previously to measure the $HgBr^*(B)$ state production. A magnetically collimated electron beam (1-200 eV) is crossed by a molecular beam of $HgBr_2$. The apparatus permits simultaneous measurements of negative ion, positive ion, and wavelength resolved photon production from $HgBr_2$. Equivalent measurements can also be made for reference permanent gases. Helium is used for this purpose since a number of line emission cross sections in the relevant wavelength region have been accurately measured by Van Zyl et al. (1980). This method of calibrating the apparatus makes it possible to measure the ratio of the emission cross section to the total ionization cross section for any other gas, provided the wavelength dependence of the relative quantum efficiency of the optical detection system and the relative ion collection efficiency are known.

Inelastic energy loss processes can be detected at threshold via collection of the resulting low energy electrons e', from the reaction

$$e + HgBr_2 \rightarrow HgBr_2^* + e' \qquad (2)$$

using the trapped electron technique. Here the potentials of the various electrodes controlling the space potential in the interaction region are arranged to give a potential well of typically a few tenths of a volt. Inelastically scattered electrons having energies less than the well depth are trapped, and are subsequently collected on a suitable biassed electrode, giving a "trapped electron signal."

1.2 Accomplishemnts

The photon counting system has been modified by replacing the photomultiplier used previously (RCA 8575) with one (RCA C31024A) having a quartz faceplate, giving much better sensitivity in the short wavelength region (~ 290 nm) where the $HgBr^*$ (C-X) emission appears. Using two standard lamps the relative photon counting efficiency of the modified system was remeasured for two interchangeable gratings blazed respectively at 300 nm and 600 nm. The resulting overall response allows use of the system for quantitative measurements from 240 nm to beyond 550 nm. Over this range the counting efficiency varies by less than a factor of four.

The wavelength resolved emission cross section of $HgBr_2$ has been measured from 240 nm to beyond 530 nm for various electron impact energies. This range encompasses the (B-X) emission measured previously, the (C-X) band of specific present interest, and the (D-X) band appearing at the shortest wavelengths. An additional band, here labelled (B'-X), appearing on the long wavelength side of the (C-X) band, and overlapping the short wavelength tail of the (B-X) band, has been documented and correlated with other measurements in this region. Partitioning of the spectrum into bands and subsequent integration over wavelength has yielded the electron energy dependences of the total band emission cross sections for all four bands: σ_c(B-X), σ_c(C-X), σ_c(D-X), and σ_c(B'-X). The present measurements of the (B-X) band agree closely with our previous measurements, provided both sets of data are calibrated in the same way. Based on more extensive He line emission measurements a revised calibration procedure has been adopted. This procedure, together with a more systematic approach to partitioning the (B'-X) and (B-X) emissions where they overlap, gives a 30% reduction in the derived (B-X) emission cross section in the plateau region compared to the values derived previously from our measurements.

A few exploratory trapped electron measurements have been performed. The main feature observed between 2 and 12 eV is a peak having a threshold at approximately 7.4 eV, consistent with the appearance potential of the lumped continuum emission cross section $\Sigma\sigma_c$(B',C,D). The onset of the (B-X) emission cross section at 6.0 eV is also obvious in the trapped electron signal. In addition, inelastic thresholds at 9.15 eV, 5.1 eV, and at approximately 3.7 eV have been observed.

2. INTRODUCTION

The objectives of the present program were to (i) measure the shape and magnitude of the cross section for dissociative excitation of $HgBr_2$ into the $HgBr^*(C^2\pi_{1/2})$ state, i.e.,

$$e + HgBr_2 \rightarrow HgBr^*(C^2\pi_{1/2}) + Br + e \qquad (1)$$

and (ii) to measure threshold energies for other inelastic energy loss processes. In a previous program, supported by the Office of Naval Research under contract N00014-81-C-0518 the cross section for production of the $HgBr^*(B^2\Sigma^+{}_{1/2})$ state by dissociative excitation of $HgBr_2$ was measured using basically the same equipment. This process is the predominant mechanism for discharge pumping of the upper laser level in the HgBr laser. The provision of these various cross sections is expected to allow more definitive modelling calculations of laser efficiency and optimum operating conditions, since in typical laser gas mixtures the collision processes controlling the electron energy distribution function are primarily those involving $HgBr_2$.

A detailed description of the apparatus and experimental technique used for the present measurements has been given previously (Chantry and Chen, 1982). In this report we confine ourselves to a description of the modifications made to the photon counting system to extend its sensitivity to shorter wavelengths.

The methods used for data analysis are described fully. They are basically the same as used previously, except that the present work necessitated a more general approach permitting the correlation of data obtained with different configurations of the photon counting system.

In the presentation of the results we include for completeness the data reported previously (Chantry & Chen, 1982) on the cross section for production of the HgBr*($B^2\Sigma^+_{1/2}$) state from $HgBr_2$.

The emission from this state extends from a well defined limit at 510 nm to a tail whose extent depends on the electron impact energy. At higher energies this tail merges with other features in the region of 300 nm. There appear to be three bands in this general region. They are clearly visible in the data of Wieland (1932), although only two of them are labeled by Wieland. That extending from 240 to 270 nm he labelled D; that from 270-295 he labelled C, and this has been assumed to arise from radiative decay of the HgBr*($C\ ^2\pi_{1/2}$) state. The third feature is a broad peak at 305 nm, with possibly a structured tail extending to longer wavelengths. The origin of this feature is not known, and does not appear to have been discussed by previous workers. For convenience we shall label it B'. Thus in all there are four distinct features to the fluorescence spectrum, which extends from 240 to 510 nm. In the present work quantitative measurements have been made of the wavelength resolved emission cross section over this entire range. This represents the basic data generated by the experiment. Division of the data into emission bands, and by integration over each band the determination of total band emission cross sections, has been performed. However, this latter step requires somewhat subjective judgements, particularly regarding the separation of the B and B' continua. Thus the emission cross section data obtained in the present program encompasses that for the dissociative excitation of HgBr*($C\ ^2\pi_{1/2}$), but is not limited to it.

3. EXPERIMENT

3.1 General Approach

The various problems attending the measurement of an independent absolute emission cross section are discussed in detail in the excellent paper by Van Zyl et al. (1980). Two aspects of such a measurement present particularly difficult problems in the present context - (i) the measurement of the absolute number density of the $HgBr_2$ molecules in the interaction region, and (ii) the absolute calibration of the optical detection system. In the present work we avoid many of these difficulties by (i) using measurements of the positive ions produced in the interaction region as a measure of the neutral gas number density and (ii) using emission measurements in Helium to calibrate the optical detection system, using particularly the "benchmark" emission cross sections determined by Van Zyl et al. (1980). In addition the relative wavelength dependence of the optical detection system is determined using two standard (deuterium and quartz halogen) lamps to cover the wavelength range of interest (240-600 nm).

The configuration of the experiment is represented schematically in Figure 1. The gas under study is introduced into the collision region in the form of a molecular beam, directed vertically downward into the throat of a liquid nitrogen cooled baffle, placed above an oil diffusion pump. A magnetically collimated electron beam travels perpendicularly through the molecular beam such that they interact in the central region of a "collision chamber." In a direction orthogonal to both beams the interaction region is viewed through aligned slits in the ion repeller plate and the containing box, which together with the ion attractor plate constitute the collision chamber. The interaction region is focussed on the entrance slit of a grating monochromator whose exit slit is focussed on the photocathode of a cooled photomultiplier operated as a photon counter.

The "ion attractor" and "ion repeller" electrodes shown in Figure 1 are electrically isolated parallel plates mounted within the collision chamber. By appropriately biassing these electrodes relative to the collision chamber box it is possible to collect and measure both positive and negative ions produced by the interaction of the crossed electron and molecular beams. Details of the various components have been described previously (Chantry & Chen, 1982). In the following subsections we describe only those components which have been modified for the purposes of the present series of measurements. No changes were made in the electrode structure, the molecular beam head, or the material handling system.

3.2 Photon Counting System

The optical system used for the present measurements is shown to scale in Figure 2. The basic arrangement is identical to that used previously (Chantry and Chen, 1982) but a number of details have been changed. In the previous work the objective was to measure radiation between 300 and 510 nm. The combination of an 1180 grooves/mm grating blazed at 600 nm and an RCA 8575 photomultiplier gave an overall relative quantum efficiency whose wavelength dependence was well matched to the above range. For the present purposes, however, it was necessary to extend the range of useful sensitivity to at least 270 nm and preferably lower. Therefore the photomultiplier was changed to an RCA C31024 equipped with a quartz window. Used in combination with a 2360 grooves/mm grating blazed at 300 nm, this gives a relative quantum efficiency which is flat within a factor of two between 480 nm and 275 nm, and at 240 nm has fallen by a factor of only 4 from its peak value (see Figure 3). This response is very adequate for the present measurements. The long wavelength limit of usefulness of this grating (~ 480 nm) is determined by the mechanical span of the monochromator drive mechanism. Measurements at longer wavelengths can be made with the 1180 grooves/mm grating blazed at 600 nm, used previously. The monochromator has a dual grating mount which facilitates rapid interchange of gratings without opening the enclosure.

An 1180 groove/mm grating blazed at 300 nm would in principle have allowed the whole wavelength range of interest (240 nm to 510 nm) to be measured using a single grating. Initial attempts to adopt this approach had to be abandoned due to inadequacies in the available gratings. Two such gratings were tested using our standard lamps system calibration procedure. Both exhibited large "ghost" responses in the region of 300 nm, rendering them unusable, at least for our particular measurements. Hence, for the actual measurements the two gratings originally provided with the monochromator [2360 grooves/mm blazed at 300 nm, and 1180 grooves/mm blazed at 600 nm] were reinstalled and used in conjunction with the new photomultiplier [RCA C31024]. In the course of demounting and remounting the various gratings the whole monochromator grating alignment and scale calibration procedure was performed. This provided a slight improvement in the system response relative to its performance in the previous series of measurement.

The new photomultiplier was mounted such that its front face occupied the same position as that of the previously used tube. To achieve this the tube socket assembly [RCA P/N AJ 2175 A], designed specifically for use with this tube, had to be carefully adapted to the thermoelectrically cooled housing. In other respects the new photomultiplier was operated as previously. Its output pulses were detected by an Ortec 9301 preamplifier (X10 coupled directly to the anode of the photomultipler, followed by an amplifier-discriminator (Ortec Model 9302) operated with a gain of ten. With this arrangement the optimum signal to dark counts ratio was achieved with 2400 V applied to the photomultiplier, cooled to -30^{o}C, with the pulse discriminator set at its mid-point, corresponding to a threshold of approximately 160 mV.

All other aspects of the photon counting and data acquisition system were identical to those described previously (Chantry and Chen, 1982).

3.3 Trapped Electron Technique

In the present apparatus the electrical potentials of the Repeller and Attractor electrodes shown in Figure 1 can be set independently relative to the potential of the collision chamber box which encloses them. In normal operation the average, center potential of the Repeller and Attractor is maintained negative relative to the collision chamber. This ensures that the electron beam has its minimum energy within the collision chamber so that when desired the electron energy at the interaction region can be reduced to essentially zero. In addition, measurements of negative ion signals can be made at the positively biassed electrode without interference from scattered electrons, which can easily escape from the region. If, on the other hand, the center potential of the Repeller and Attractor electrodes is made positive relative to the collision chamber, we create a "potential well" within the chamber. Any low energy electrons created in the interaction region by inelastic energy loss collisions will be unable to escape from this well if their energy is less than the well depth. As a result of further collisions they will migrate across the magnetic field lines until they are ultimately collected at the positively biassed electrode. The resulting current is referred to as a trapped electron signal. This technique was pioneered by Schulz (1958) and further refined by Burrow and Schulz (1969). With sufficient care the technique can yield absolute values for the energy loss cross section in the immediate vicinity of the threshold, provided a unique energy loss is involved. At each new threshold the trapped electron signal starts to increase, and reaches a peak at an energy above threshold equal to the well depth. Thus the relative peak height in the trapped electron signal tends to be proportional to the magnitude of the inelastic cross section at an energy above threshold equal to the well depth. In the course of the present program exploratory measurements of this type were performed in $HgBr_2$ in order to provide additional information on the thresholds and relative cross section magnitudes near threshold for all inelastic energy loss processes, including those producing radiation.

4. DATA ANALYSIS

4.1 Cross Section Ratios

The underlying principle of the present experiment is that measurements in a known gas (He) are used to calibrate the system such that in an unknown gas we are able to determine the ratio of the emission cross section to the ionization cross section. An additional minor complication in the present case is that the calibration is performed with line emission, while the "unknown" emission is in the form of a continuum. In the following analysis it is convenient to characterize quantities measured in the calibrating gas by the subscript "ℓ" (i.e., line), while those relevant to the "unknown" gas have the subscript "c" (i.e., continuum). The various symbols used in the analysis are listed in Table 1 together with their definitions.

In the line emitting calibrating gas it follows from the definitions that

$$e\dot{N}_\ell(\lambda_\ell,\varepsilon_\ell) = E(\lambda_\ell)I_eN_\ell L\sigma_\ell(\lambda_\ell,\varepsilon_\ell) \tag{3}$$

$$I^{+}_\ell(\varepsilon_{i\ell}) = E^{+}_\ell(\varepsilon_{i\ell})I_eN_\ell L\sigma_{i\ell}(\varepsilon_{i\ell}) \tag{4}$$

We may write the ratio of Equations (3) and (4) in the form

$$\frac{I^{+}_\ell(\varepsilon_{i\ell})}{e\dot{N}_\ell(\lambda_\ell,\varepsilon_\ell)} \cdot \frac{E(\lambda_\ell)}{E^{+}_\ell(\varepsilon_{i\ell})} \cdot \frac{\sigma_\ell(\lambda_\ell,\varepsilon_\ell)}{\sigma_{i\ell}(\varepsilon_{i\ell})} = 1 \tag{5}$$

Similarly, for the continuum emitting gas we write

$$e\,\dot{N}_c(\lambda_o,\varepsilon_c) = I_e N_c L \int E(\lambda)\sigma_c(\lambda,\varepsilon_c)F_{sc}(\lambda-\lambda_o)\,d\lambda \qquad (6)$$

and

$$I_c^+(\varepsilon_{1c}) = E_c^+(\varepsilon_{1c}) I_e N_c L \sigma_{1c}(\varepsilon_{1c}) \qquad (7)$$

With the assumption that $E(\lambda)$ and $\sigma_c(\lambda,\varepsilon_c)$ are essentially constant over the width W_{sc} of the slit function $F_{sc}(\lambda-\lambda_o)$ we may approximate Equation (6) by

$$e\,\dot{N}_c(\lambda_o,\varepsilon_c) = I_e N_c L\, E(\lambda_o)\sigma_c(\lambda_o,\varepsilon_c)W_{sc} \qquad (8)$$

where

$$W_{sc} = \int F_{sc}(\lambda-\lambda_o)\,d\lambda \qquad (9)$$

is the effective width of the slit function. For a triangular slit function W_{sc} is simply the full width at half maximum (FWHM). By definition, $F(0) = 1$.

The ratio of Equations (7) and (8) gives

$$\frac{\sigma_c(\lambda_o,\varepsilon_c)}{\sigma_{1c}(\varepsilon_{1c})} = \frac{e}{W_{sc}} \cdot \frac{E_c^+(\varepsilon_{1c})}{E(\lambda_o)} \cdot \frac{\dot{N}_c(\lambda_o,\varepsilon_c)}{I_c^+(\varepsilon_{1c})} \qquad (10)$$

Multiplying Equation (10) by Equation (5) gives

$$\frac{\sigma_c(\lambda_o,\varepsilon_c)}{\sigma_{1c}(\varepsilon_{1c})} = R^+ \left[\frac{\sigma_\ell(\lambda_\ell,\varepsilon_\ell)}{\sigma_{1\ell}(\varepsilon_{1\ell})}\right]\left[\frac{I_\ell^+(\varepsilon_{1\ell})\,R(\lambda_\ell)}{\dot{N}(\lambda_\ell,\varepsilon_\ell)}\right]\left[\frac{\dot{N}_c(\lambda_o,\varepsilon_c)}{I_c^+(\varepsilon_{1c})\,R(\lambda_o)}\right]\left[\frac{1}{W_{sc}}\right] \qquad (11)$$

where

$$R^+ = \frac{E_c^+(\varepsilon_{1c})}{E_\ell^+(\varepsilon_{1\ell})} \qquad (12)$$

is the relative ion collection efficiency

and
$$R(\lambda_o) = \frac{E(\lambda_o)}{E(\text{ref})} \tag{13}$$

is the relative quantum efficiency (RQE) at wavelength λ_o obtained by normalization to a conveniently chosen reference value E(ref) and $R(\lambda_\ell)$ is defined similarly.

Integrating Equation (11) over wavelength λ_o gives the ratio of total continuum emission cross section

$$\sigma_c(\varepsilon_c) = \int \sigma_c(\lambda_o,\varepsilon_c)d\lambda_o \tag{14}$$

to the ionization cross section

$$\frac{\sigma_c(\varepsilon_c)}{\sigma_{ic}(\varepsilon_{ic})} = R^+\left[\frac{\sigma_\ell(\lambda_\ell,\varepsilon_\ell)}{\sigma_{i\ell}(\varepsilon_{i\ell})}\right]\left[\frac{I_\ell^+(\varepsilon_{i\ell})\ R(\lambda_\ell)}{\dot{N}(\lambda_\ell,\varepsilon_\ell)}\right]\left[\frac{1}{W_{sc}}\int\frac{\dot{N}_c(\lambda_o,\varepsilon_c)\ d\lambda_o}{R(\lambda_o)\ I_c^+(\varepsilon_{ic})}\right] \tag{15}$$

The positive ion current measured in the continuum case is retained within the integral in recognition of the possible variation of neutral beam density during the measurement of $\dot{N}_c(\lambda_o,\varepsilon_c)$ over the necessary wavelength region. In the present experiment the wavelength dependence of $\dot{N}_c(\lambda_o,\varepsilon_c)$ is measured at fixed energy ε_c by scanning the monochromator at constant speed S nm/sec, and storing the resulting counts in the multi-channel scaler where each channel has the corresponding width W_{ch} in nm. If the counts accumulated in channel n number $N_c(n)$, and the center wavelength of the channel is λ_n, then we may write

$$\dot{N}_c(\lambda_n) = \frac{S[N_c(n)-B(n)]}{W_{ch}} \tag{16}$$

for substitution into Equation (11).

Similarly, in Equation (15) we replace the integral by the summation

$$S \sum \frac{[N_c(n)-B(n)]}{R(\lambda_n)I_c^{+}(\varepsilon_{1c})} \tag{17}$$

where we have corrected the signal for background. Hence, for final working formulae we arrive at

$$\frac{\sigma_c(\lambda_n,\varepsilon_c)}{\sigma_{1c}(\varepsilon_{1c})} = \frac{A}{W_{ch}} \left[\frac{N_c(n)-B(n)}{R(\lambda_n)I_c^{+}(\varepsilon_{1c},n)}\right] \tag{18}$$

$$\frac{\sigma_c(\varepsilon_c)}{\sigma_{1c}(\varepsilon_{1c})} = A \sum \left[\frac{N_c(n)-B(n)}{R(\lambda_n)I_c^{+}(\varepsilon_{1c},n)}\right] \tag{19}$$

where

$$A = \left[\frac{\sigma_\ell(\lambda_\ell,\varepsilon_\ell)}{\sigma_{1\ell}(\varepsilon_{1\ell})}\right]\left[\frac{R^{+}R(\lambda_\ell)}{W_{sc}}\right]\left[\frac{I_\ell^{+}(\varepsilon_{1\ell})}{\dot{N}_\ell(\lambda_\ell,\varepsilon_\ell)}\right] S \tag{20}$$

For each wavelength scan of the continuum A is a constant of the instrument. In Equation (20) the quantities in the first bracket are taken from the literature, those in the second are experimental parameters depending on the operating conditions, and must be measured, and those in the final bracket are directly measured quantities. The scanning speed, S, is a preset parameter.

4.2 Effective Slit Function Width, W_s

The effective width, W_s, of the normalized slit function is determined by the dispersion of the grating and the geometric width of the slits of the monochromator. It can easily be measured by scanning a line whose true width is much smaller than W_s using a channel width $W_{ch} << W_s$. Under these conditions

$$W_s = \frac{W_{ch} \sum [N_\ell(n)-B(n)]}{N_\ell(n_\ell)-B(n_\ell)} \tag{21}$$

where n_ℓ is the channel number corresponding to λ_ℓ, and the summation encompasses an appropriate number of channels on each side of n_ℓ.

4.3 Relative Quantum Efficiency, R(λ)

In order to evaluate Equation (18) and (19) it is necessary to know the relative quantum efficiencies of the photon counting system in the configurations used for the continuum measurements [i.e., $R(\lambda_n)$], and for the line emission measurements being used for data normalization [i.e., $R(\lambda_\ell)$]. The definition of R(λ) is given by Equation (13) which in general may be written

$$R_i(\lambda) = \frac{E_i(\lambda)}{E(\mathrm{ref})} \qquad (22)$$

where the subscript i indicates a specific configuration of the photon counting system. In general the magnitude and shape of E(λ) will depend on the choice of (i) the monochromator grating and (ii) the photomultiplier. Changes in (iii) the monochromator alignment, (iv) the monochromator slits and (v) the operating conditions of the photomultiplier will affect the magnitude of E(λ), but should not affect the shape. In practice the operating conditions of the photomultipliers have not been varied, and the monochromator alignment has been changed only once, at the outset of the present series of measurements. Hence we are primarily concerned with different combinations of the remaining three factors.

For each combination of grating and photomultiplier the system has been calibrated using standard lamps. The photon count rate recorded at a monochromator setting λ_o may be represented by

$$\dot{N}_L(\lambda_o) = G \int E(\lambda)\, L(\lambda)\, F_s(\lambda-\lambda_o)\, d\lambda \qquad (23)$$

where L(λ) is the lamp spectral irradiance function in units of photons/cm^2-nm, and G is a geometrical factor depending on the optical coupling of the lamp to the system. Assuming that any variation of E(λ) and $L(\lambda)$ over the extent of the slit function $F_s(\lambda-\lambda_o)$ is linear, and that $F_s(\lambda-\lambda_o)$ is a symmetrical function about λ_o, we may approximate Equation (23) by

$$\dot{N}_L(\lambda_o) = G\ E(\lambda_o)L(\lambda_o)\ W_s$$

giving

$$E(\lambda_o) = \frac{\dot{N}_L(\lambda_o)}{G\ L(\lambda_o)\ W_s} \qquad (24)$$

where W_s is defined by Equation (9).

It is clear from Equation (24) that the shape of the $E(\lambda)$ function (and its corresponding $R(\lambda)$ function) can be obtained by plotting $N_L(\lambda_o)/L(\lambda_o)$ as a function of monochromator setting λ_o. To determine the relative magnitudes of values of $E(\lambda)$ appropriate to different system configurations we must evaluate the ratio

$$\frac{E_1(\lambda_1)}{E_2(\lambda_2)} = \left[\frac{\dot{N}_{L,1}(\lambda_1)}{\dot{N}_{L,2}(\lambda_2)}\right]\left[\frac{G_2}{G_1}\right]\left[\frac{L(\lambda_2)}{L(\lambda_1)}\right]\left[\frac{W_{s2}}{W_{s1}}\right] \qquad (25)$$

where subscripts 1,2 indicate different system configurations. In order to use Equation (25) it is convenient to fix the value of G by maintaining the same optical coupling between the lamp and the detector. The ratio $L(\lambda_2)/L(\lambda_1)$ is derived from the calibration data supplied with the lamp, or made unity by comparing measurements where $\lambda_1 = \lambda_2$. With these constraints Equation (25) reduces to

$$\frac{E_1(\lambda)}{E_2(\lambda)} = \left[\frac{\dot{N}_{c,1}(\lambda)}{\dot{N}_{c,2}(\lambda)}\right]\left[\frac{W_{s2}}{W_{s1}}\right] \qquad (26)$$

where subscript "L" has been replaced by "C", indicating that any continuum source will suffice for such a measurement.

Alternatively, if a narrow line source is available a direct comparison of the line emission signals suffices, since

$$\frac{E_1(\lambda_\ell)}{E_2(\lambda_\ell)} = \frac{\dot{N}_{\ell,1}(\lambda_\ell)}{\dot{N}_{\ell,2}(\lambda_\ell)} \tag{27}$$

5. RESULTS

5.1 Wavelength Dependence of the Relative Quantum Detection Efficiency

In this subsection we describe the methods used to determine the function

$$R(\lambda_o) = \frac{E(\lambda_o)}{E(ref)} \qquad (13)$$

where λ_o is the corrected wavelength setting of the monochromator, and $E(\lambda_o)$ is the photon counting efficiency of the system for photons of wavelength λ_o. As discussed in Section 4.1, any convenient value of E(ref) may be used for normalization. For consistency with our previous measurements (Chantry and Chen, 1982) we use the value obtained previously at 504.8 nm using the 1180 g/mm grating blazed at 600 nm, with 500 μm slits, and the RCA 8575 photomultiplier operated under the previously specified conditions (C'500 in Table 2).

For present purposes it was necessary to measure $R(\lambda_o)$ for the configuration A (see Figure 3) of the photon counting system, from 240 nm to at least 416.9 nm, this being the shortest wavelength "benchmark" He emission line cross section available (Van Zyl et al., 1980). While this range would have sufficed for the measurement of the C-X fluorescence band, it was clearly desirable to extend the range of measurement to include the previously measured B-X band. This required the use of two gratings, as explained in Section 3.2, allowing measurements to extend from 240 nm to beyond 510 nm. Measurements of $R(\lambda_o)$ over this range necessitated the use of two standard lamps. For the shorter wavelengths a deuterium arc discharge lamp,* calibrated over

---

Optronic Laboratories, Inc. Model UV-40 the range 180 to 400 nm, was used. Scans of the output were performed over the range 250 to 400 nm. For longer wavelengths a tungsten halogen filament lamp was used. The calibration data supplied with this lamp extends from 250 to 2500 nm. For the present purposes, however, scans were performed only from 250 to 650 nm.

The procedures adopted in performing the standard lamp calibration measurements have been previously described [Chantry & Chen, 1982]. As a check on the reproducibility of these procedures, and in order to relate the present series of measurements with our earlier B-X fluorescence measurements, the system response $R(\lambda_0)$ was also remeasured for the original configuration. The result, shown as Curve C in Figure 3, differs insignificantly in shape from the one obtained previously [see Figure 9 of Chantry & Chen, 1982]. The present curve's magnitude has, however, been adjusted to give a value of 1.04 at 504.8 nm, based on a measured improvement in the effective width W_s of the "slit" function, from a previous value of 1.80 nm to the present value of 1.73 nm, using 500 μm slits. This improvement resulted from realignment of the grating.

All three curves shown in Figure 3 were measured by the procedure described previously. A number of scans were made with each configuration/lamp combination in order to demonstrate reproducibility of the curves. In some cases particular care was taken to maintain constant optical coupling of the standard lamp to the system for data taken with all three configurations. These particular sets of data thus determine the shapes of curves in Figure 3, and their vertical (logarithmic) displacement from each other. In comparing the performance of configuration A with B and/or C account had to be taken, using Equation (26), of the different effective width W_s of the slit function, due to the different groove density of the UV blazed grating. For this purpose apparent line shape measurements were performed for each of the relevant configurations, using a number of different He emission

---

*The Eppley Laboratory, Inc. Model ES-8203 lines. An example of this type of measurement, performed with configuration A and 1000 μm slits, is shown in Figure 4. The resulting value of W_s = 1.65 nm is listed in Table 2 together with other values determined similarly. Configurations A, B and C apply to the system after realignment of the monochromator gratings had been performed. Prior to realignment a value of 1.80 nm had been measured for configuration C, with 500 μm slits, as reported previously [Chantry and Chen, 1982]. This is listed as Configuration C'500.

In order to confirm the relationship of curves A and B in Figure 3 resulting from the above procedures, intensity measurements were made for seven He emission lines, at 294.5, 318.8, 388.9, 396.5, 412.1, 447.2 and 471.3 nm. Line emission signals were measured with both gratings under otherwise identical conditions. At each wavelength, the ratio of the signals should correspond to the logarithmic separation of curves A and B. This was found to be so, within a few percent, for most of the lines used. The worst discrepancy was 10%. This agreement was considered acceptable.

The same type of measurement, i.e., the measurement of the ratio of He line emission signals, was used to establish the effect, on the R(λ) curves of Figure 3, of increasing the slit widths from 500 μm to 1000 μms. This was found to increase the line emission signals by a factor of 2.20. In using the curves of Figure 3 to interpret measurements made with the wider slits, using for example Equation (18-20), this factor must be included.

5.2 Helium Line Calibration Data

The objective of these particular measurements was to evaluate the quantity

$$R(\lambda_\ell) \left[\frac{\sigma_\ell(\lambda_\ell,\varepsilon_\ell)}{\sigma_{1\ell}(\varepsilon_{1\ell})} \cdot \frac{I^+_\ell(\varepsilon_{1\ell})}{\dot{N}_\ell(\lambda_\ell,\varepsilon_\ell)}\right] \qquad (28)$$

appearing in the "instrument constant" A defined by Equation (20). Because of its proximity to the peak of the HgBr(C-X) fluorescence the He 416.9 nm (6^1S-2^1P) line was chosen initially as the reference calibration line, with the He 443.8 nm (5^1S-2^1P) and He 504.8 nm (4^1S-2^1P) lines providing additional calibration points. All three lines were included in the benchmark cross section measurements of Van Zyl et al. (1980). The relevant quantities from this publication, and that of Rapp & Englander-Golden (1965) are listed in Table 3. Note that it was necessary to obtain the line emission cross section at 150 eV by interpolation between values given for 100 eV and 500 eV. Also, the values listed for 35 eV are those derived previously by us [Chantry and Chen, 1982].

Measurements of the line emission signals for all three benchmark lines were performed using configuration B500. The results are summarized in Table 4. In addition, measurements were made of the 416.9 nm and 443.8 nm signals using configurations A500 and A1000, summarized in Table 5. The values of $R(\lambda_\ell)$ used in these tables are shown in the first column. They were read from the appropriate curves plotted in Figure 3. The values for Table 5 include where appropriate the factor 2.20 for 1000 μm slits, as discussed in Section 3.1. The cross section ratio listed in the third column of the tables is obtained from the reference data listed in Table 3. The pressure listed in the fourth column is the Baratron reading for each measurement. The location of the Baratron is such that it indicates the pressure at a point considerably upstream in the gas inlet line. Its reading is proportional to, but much larger than the true pressure, or rather beam density, in the collision region. The reading does not enter into the calculation of cross sections, and is included here primarily for purposes of reference. We have previously established [Chantry and Chen, 1982] that the ion currents and the photon count rates corrected for background are directly proportional to both the pressure indicated by the Baratron gauge, and the measured transmitted electron current. The data in Tables 4 and 5 all corresponds to an electron current of 2 × 10^{-5}A -- a value well within the demonstrated range of linearity.

The fifth and sixth columns of the tables show the measured ion current and photon count rate, respectively. The latter quantity has been corrected for background, B_ℓ, recorded by electrostatically reflecting the electron beam before it enters the collision region, but keeping the filament heating conditions identical to those employed in the measurements.

In principle all the measurements shown in Tables 4 and 5 should give the same value for the quantity listed in the final column. For a particular line measurement, any systematic dependence of this quantity on electron energy (ε_ℓ) would indicate a systematic discrepancy between the present measurements and those of Van Zyl et al (1980), regarding the <u>shape</u> of the cross section. No such discrepancies are apparent. Systematic variations of the final column number for the same line, but different optical configurations (i.e., between tables) would indicate systematic errors in the $R(\lambda_\ell)$ values employed. Such systematic variations are not apparent from the tabulated data.

We note in Table 4 that the 504.8 nm data gives a final column quantity which is systematically about 20% larger than the remaining data. The root of this discrepancy cannot be traced at present. Van Zyl et al. (1980) indicate high confidence level uncertainties of typically ± 10% or better for these cross sections, and we would expect the relative values to be less uncertain than the quoted uncertainties in their absolute values.

For the present purposes, of calibrating HgBr data taken primarily with configuration A1000, we elect to use a value of 2.00 (-14) amp. sec. for the final column quantity of Tables 4 and 5. This is the average of all the values measured for the 416.9 nm and 443.8 nm lines.

5.3 Relative Ion Collection Efficiencies

In the present measurements identical ion extraction voltages were used, and the same electron energy (50 eV) was used to monitor the $HgBr_2$ density, as in the previous measurments. The previously determined value of

$$R^+ = \frac{E_c^+(HgBr_2, 50.\mathrm{ev})}{E_\ell^+(He)} = 0.81 \pm 0.05 \qquad (29)$$

was confirmed by repetition of the measurements described previously [Chantry and Chen, 1982].

5.4 Optical Emission Measurements in $HgBr_2$

The procedures employed for the present measurements are basically the same as those described previously [Chantry and Chen, 1982]. Most of the measurements employed optical configuration A1000 (see Table 2), since this gave adequate resolution for the He line calibration measurements at 416.9 and 443.8 nm, described in Section 5.2, and has the necessary response at short wavelengths. As previously the electron energy scale correction was determined from the positive ion appearance potential (10.60 eV), and the wavelength scale was calibrated via the known Hg lines appearing in the spectrum when the electron energy exceeded 10 eV. Most wavelength scans extended from 240 nm to 440 nm and occupied the full 400 channels of the multichannel scaler (MCS). These scans encompassed the (D-X), the (C-X), and the (B'-X) emission bands, as well as part of the (B-X) band measured previously. In addition, a few scans were recorded using optical configuration B1000 (see Table 2), and covering the range 251.5 nm to beyond 530 nm. These scans provide data which allows evaluation of the B-X emission cross section for direct comparisons with our previous measurements.

Examples of the raw data obtained by scanning the monochromator wavelength synchronously with the MCS, using the A1000 optical configuration, are shown in Figure 5. The mercury emission lines are clearly visible in the higher energy data, and provide a direct calibration of the wavelength scale. Data runs of this type were made at the various electron energies, spanning the range from threshold to 35 eV. Each set of data was corrected point by point for background signal and for relative quantum efficiency, and then replotted. Some examples of smooth curves drawn through the resulting data are shown in Figure 6. In these plots the Hg emission lines have been removed by smoothly connecting the adjacent regions of the continuum. The absolute cross section scale of Figure 6 was obtained via Equation (18), using the value of 1.85×10^{-15} cm^2 (Wiegand and Boedeker, 1982) for the $HgBr_2$ ionization cross section at the reference energy (50 eV).

Three distinct bands are visible in Figures 5 and 6. Following the notation of Wieland (1932) and subsequent workers (e.g., Wadt, 1980), we assume that the bands peaking at 258 and 288 nm arise from $HgBr^*$(D-X) and $HgBr^*$(C-X) transitions. The band peaking at 305 nm apparently has received little or no discussion in the literature, although it is clearly visible in the spectrum published by Wieland (1932), and in the spectrum produced by reaction of $Xe^*(^3P_2)$ with $HgBr_2$, published recently by Dreiling and Setser (1983). An analogous band has been reported in HgI^* by Roxlo and Mandl (1980). For purposes of discussion we refer to this region as the (B'-X) band with the implied assumption that, in common with the other bands, it arises from dissociative excitation of $HgBr_2$, and a transition to the ground state (X) of HgBr.

The first order dependence of all three bands on the $HgBr_2$ neutral beam density has been established by operating the reservoir at a number of set temperatures and recording the photon count rates at monochromator settings close to each peak, using 10 eV electron beam energy, together with the ion current measured at 50 eV electron energy. The resulting data is shown in Figure 7. The lines fitted to the data have been drawn with a slope of unity, indicating that the photon production processes have the same order dependence on $HgBr_2$ density as does the ionization process. The latter is known to be first order.

In order to extract total continuum emission cross sections from data of the type shown in Figure 6 it is necessary to partition the signal into contributions to the four continua. It is impossible to do this with complete confidence, and different interpretations of the data which conserve the total emission cross section of all bands are conceivable. In these circumstances we have chosen a well defined simple method of partitioning the data, illustrated in Figures 8 and 9.

The boundary between the (D-X) band and the (C-X) band has been set at 270.5 nm, where the minimum signal is observed at essentially all electron energies. All signal between 242.5 and 270 nm is assigned to the D-X emission band. Similarly, all signal between 270.5 nm and 295.5 nm is assigned to the C-X band. The most difficult partition to rationalize is between the (B'-X) band and the (B-X) band. At energies close to the threshold for production of the peak at 305 nm the short wavelength tail of the (B-X) continuum may reasonably be extrapolated to zero at 295.5 nm as indicated in Figure 8. As the energy is raised structure appears on the continuum, between the peak at 305 nm, and extending to longer wavelengths. Since growth of this structure appears to accompany the growth of the 305 nm peak, we postulate that they are part of the same band. Based on these observations we have chosen to consistently extract the (B-X) signal by assuming that it increases linearly from zero at 296 nm to a value at 412.5 nm equal to the full measured signal. All the signal between 412.5 nm and ~ 530 nm is assigned to the B-X band. The net effect of this partitioning procedure is seen in Figure 9 for the case of $\varepsilon = 8.0$ eV.

The method used with the present data systematically assigns a smaller overall signal to the (B-X) continuum than the method used by us previously [Chantry and Chen, 1982], where all the continuum signal between ~ 350 nm and ~ 530 nm was assigned to the (B-X) band, and a smooth extrapolation used to zero at ~ 290 nm. See for example, Figure 13 of Chantry and Chen (1982).

Using the partitioning procedures defined above the wavelength resolved data of the type represented in Figures 6, 8 and 9 has been used to calculate the total continuum cross sections for the various emission bands, using Equation (19) to integrate between appropriate wavelengths. The results are shown in Figure 10 for the (B'-X), (C-X), and (D-X) total continuum emission cross section. In this figure the filled points have been obtained by the complete integration procedure. The open points were obtained by measuring the signal at the peak wavelength 257, 288 and 305 nm and scaling the resulting curve to match the filled points in the region of overlap. Note the change of scale at 30 eV in Figure 10.

The curves shown in Figure 10 below 30 eV were obtained by tuning the monochromator to the peak wavelengths, and scanning the electron energy synchronously with the MCS. So far as we can determine from this data, for each of the three bands representation in Figure 10 the wavelength resolved cross section at each peak has an electron energy dependence identical to that of the total continuum emission of that band. This is not the case for the (B-X) band, as shown in Figure 14 of Chantry and Chen (1982).

Measurements of the thresholds for appearance of radiation at the peak wavelengths gave values of 7.45 eV at 307 nm, 7.40 eV at 288 nm, and 7.65 eV at 258 nm. The first two of these are the same within the limits of error of ± 0.1 eV.

The cross sections shown in Figure 10 are shown again in Figure 11 together with the (B-X) total emission cross section. The latter data is a composite of present data obtained with Configuration B1000, and previously determined data [Chantry and Chen, 1982], reanalyzed according to the partitioning procedure and scaled via the benchmark cross sections at 416.9 nm and 443.8 nm. All the data forms a self-consistent set. Differences between the present (B-X) cross section magnitude and the previously derived cross section arise entirely from the revised method of interpretation and scaling.

For purposes of calculating electron energy distribution functions in mixtures where $HgBr_2$ dominates it is convenient to lump together the three cross sections represented in Figure 10, to give a single energy loss cross section having a threshold at 7.4 eV. This lumped cross section is also shown in Figure 11. The similarity of shape of the three contributing cross sections may well be an indication that production of all three bands involves electron impact excitation of the same intermediate state of $HgBr_2^*$. If this is the case, the lumped cross section shown in Figure 11 is a lower bound to the cross section for excitation of the intermediate state.

5.5 Trapped Electron Measurements in $HgBr_2$

In the course of the present program the opportunity was taken to make some exploratory measurements of trapped electron signals in $HgBr_2$. Only a few such measurements were made, and in the absence of accompanying systematic measurements (Burrow and Schulz, 1969), required to establish the effective well depth we are not able to interpret the data in terms of absolute excitation cross sections. The data is, however, instructive regarding the relative magnitudes of the inelastic energy loss cross sections close to their thresholds, particularly when viewed in the context of the optical emission cross sections reported above, and the energy loss spectrum published by Spence et al. (1982) for 200 eV electrons scattered at 3^o.

In the present measurements the well depth is controlled by the potentials of the Repeller and Attractor electrodes relative to the collision chamber box which encloses them - see Figure 1. For the data shown in Figure 12 the Repeller and Attractor were biassed + 4V and-2V respectively. As a result the trapped electron signal appears at the Repeller, while the positive ion signal appears at the Attractor. Both signals, measured between 2 and 12 eV electron beam energy, are displayed in Figure 12. The positive ion appearance potential (10.60 eV) has been used to calibrate the electron energy scale. The broken curve labelled I^- is an estimate of the negative ion contribution to the current collected at the Repeller, based on similar measurements performed without a potential well in the collision chamber.

The most easily identified features in the trapped electron signal are the onsets labelled B and C, which correspond to the thresholds measured optically for excitation of the $HgBr^*(B)$ state (6.0 eV), and for the lumped excitation of the $HgBr^*(B',C,D)$ states (> 7.4 eV). According to Figure 11 these emission cross sections have approximately equal slopes immediately above their respective thresholds. The trapped electon data suggests that the energy loss cross section starting at 7.4 eV rises significantly more rapidly than the 6.0 eV process. This would be consistent with the relative magnitudes proposed by various workers to fit Boltzmann and laser kinetics codes to discharge and swarm experiments (Kline et al., 1983; McGeoch et al., 1983; Nighan & Brown, 1983). This suggests that the energy loss reactions having thresholds close to 7.4 eV result to a large extent in non-radiating products.

The abrupt increase in the trapped electron signal in the region of 9.15 eV, labelled D in Figure 12, corresponds to the onset of a substantial peak in the energy loss spectrum of Spence et al. (1982). Thus there appears to be a new energy loss process threshold at approximately 9.1 eV. The near threshold cross section gradient is apparently much smaller than that of the 7.4 eV process.

The trapped electron signal below 6 eV is more difficult to interpret. There appears to be a broad peak starting at approximately 3.7 eV, after allowance is made for the negative ion contribution, with an additional onset at approximately 5.1 eV. The first, broad feature correlates approximately with the first broad feature observed by Spence et al. (1982), but the present onset at 5.1 eV has no counterpart in their "pseud-optical" spectrum. This suggests that the $HgBr_2$ electronic transition involved is optically forbidden.

6. DISCUSSION

The measurements reported here are an extension of work performed previously (Chantry & Chen, 1982) which concentrated on measuring the cross section for production of the $HgBr^*$ ($B^2\Sigma_{1/2}$) state by electron impact on $HgBr_2$. The present data set includes repetition of some of the measurements of the HgBr (B-X) emission band for direct comparison with our previous data. The wavelength resolved cross sections obtained from both sets of measurements show good agreement, typically to better than 5%, provided the same He line emission is used in the calibration procedure. In the previously reported data (e.g. Figure 13 of Chantry & Chen, 1982), the He 504.8 nm line was used for calibration. The present measurements of the He line emission signals at all three "benchmark" wavelength (416.9, 443.8, and 504.8 nm) have revealed a systematic 20% discrepancy at the longer wavelength relative to the two shorter wavelengths based on the benchmark cross sections of Van Zyl et al. Because of this discrepancy, we prefer now to base our calibration procedure on the two shorter wavelength line emission signals, which are self-consistent. Use of this revised calibration has the effect of reducing the magnitudes of the wavelength resolved cross sections determined previously, by the factor (2.00/2.40). This is the ratio of the average numbers given by the final columns of Tables 4 and 5 for the two shorter wavelength lines (2.00) and for the 504.8 nm data (2.40). The previously reported data of this type (Figure 13 of Chantry & Chen, 1982), revised in this way, is reproduced here as Figure 13 of this report.

As discussed in Section 5.4, based on the present measurements, we have also revised the method used to partition the wavelength resolved emission cross section between the (B-X) and the (B'-X) bands in the region from 296 to 412.5 nm. When systematically applied to our previous data, samples of which are shown in Figure 13, this revised procedure leads to a further reduction in the derived total band emission cross section, σ_c (B-X), for energies above 7 eV. The overall revised values of σ_c(B-X) determined from our previous data are shown by the appropriately labelled full and broken curve in Figure 11. The three filled points shown have been derived from measurements performed during the present series, using optical configuration B1000 to cover the necessary range of wavelengths.

It should perhaps be emphasized that the various cross sections plotted in Figure 11 constitute a self-consistent set. The same calibration procedure has been used for all the data represented, and at any energy the sum of the various cross sections, given by adding σ_c(B-X) to the lumped cross section labelled $\Sigma\sigma_c$(D,C,B'-X), is independent of the procedure chosen to partition the radiation between the various bands.

Most previous attempts to establish a set of $HgBr_2$ cross sections to account for discharge and swarm experiments have included inelastic energy loss processes having thresholds at 5.0, 6.4, and 7.9 eV, with the process starting at 6.4 eV being responsible for production of the $HgBr^*$(B) state. Based on the present measurements it is clear that the processes assumed to start at 6.4 and 7.9 eV do in fact start at 6.0 eV and 7.4 eV, respectively. A similar conclusion can be drawn from a proper interpretation of the energy loss spectrum of Spence et al. (1982). Inclusion of cross sections having thresholds at approximately 3.7 eV, and at 5.1 eV and 9.15 eV is suggested by the trapped electron data shown in Figure 12. However, without additional information regarding the overall shapes, and magnitudes, of those cross sections, their inclusion in the Boltzmann code analyses may not be particularly fruitful. It has been recognized from the outset in such analyses that the 5.0 eV and 7.9 eV processes are "representative" of energy loss processes, below the threshold for $HgBr^*(B)$ state production in the one case, and between this threshold and that for ionization (10.6 eV) in the other case. Provided these "representative" cross sections are suitably adjusted in magnitude, the inaccuracies in their threshold energies are probably not significant regarding predictions of the $HgBr^*(B)$ state excitation efficiency and the ionization coefficient. Similarly, quantitative predictions of the attachment coefficient and electron drift velocity measured in swarm experiments in gas mixtures containing $HgBr_2$ (Nighan et al, 1982) required the use of "representative" energy loss cross sections involving "resonant" and "direct" vibrational excitation. The present trapped electron data indicate the presence of an energy loss process starting at approximately 3.7 eV. If included in the analyses this process might be found to be significant in determining the attachment rate, although for this purpose a lower threshold would be more effective.

The present trapped electron data show no evidence for the resonant energy loss process peaking at ~ 3 eV, invoked by Nighan et al. Appearance of a trapped electron signal is however only expected if the energy losses involved are sufficiently large, approaching the initial electron energy. Thus we can only conclude that, if the resonant process is indeed present, it does not involve large energy losses. In their analysis Nighan et al. assumed an effective energy loss of 0.25 eV. Such a process at ~ 3 eV impact energy would not result in a trapped electron in any of the present measurements.

ACKNOWLEDGEMENTS

The authors are indebted to a number of their colleagues for their assistance and interest during this project. The experiment would not have been possible without the expert technical work of W. M. Uhlig, W. F. Toth and C. S. Spontak in constructing the apparatus. W. D. Partlow and J. T. Veligdan generously loaned us important optical components, and C. Hirayama provided the $HgBr_2$ capsules. L. E. Kline and C. S. Liu were participants in a number of useful discussions. The authors are also appreciative of the encouragement, interest and understanding of M. B. White of the Office of Naval Research, Boston.

This report was prepared by Toni McElhaney and the Word Processing Center.

7. REFERENCES

Burrow, P. D. and Schulz, G. J. (1969) Phys. Rev. 187, 97-105.

Chantry, P. J. and Chen, C. L. (1982) Final Report to Contract N00014-81-C-0518. Report No. 82-9C1-EXCIT-R1. Gov't. Accession No. A119583.

Dreiling, T. D. and Setser, D. W. (1983) J. Chem. Phys. 79, 5439-5444.

Kline, L. E., Chen, C. L., Chantry, P. J. and Denes, L. J. (1983) Bull. Am. Phys. Soc. 28, 179.

McGeoch, M. W., Hsia, J. C. and Klimek, D. E. (1983) J. Chem. Phys. 78, 1180-1184.

Nighan, W. L. and Brown, R. T. (1982) J. Appl. Phys. 53, 7201-7210.

Nighan, W. L., Hinchen, J. J. and Wiegand, W. J. (1982) J. Chem. Phys. 77, 3442-3452.

Rapp, D. and Englander-Golden, P. (1965) J. Chem. Phys. 43, 1464-79.

Roxlo, R. and Mandl, A. (1980) J. Chem. Phys. 72, 541-543.

Schulz, G. J. (1958) Phys. Rev. 112, 150-154.

Spence, D., Wang, R.-G. and Dillon, M. A. (1982) Appl. Phys. Lett. 41, 1021-1023.

Van Zyl, B., Dunn, G. H., Chamberlain, G. and Heddle, D.W.O. (1980) Phys. Rev. A 22, 1916-1929.

Wadt, W. R. (1979) Appl. Phys. Lett. 34, 658-660.

Wadt, W. R. (1980) J. Chem. Phys. 72, 2469-2478.

Wiegand, W. J. and Boedeker, L. R. (1982) Appl. Phys. Lett. 40, 225-227.

Wieland, K. (1932) Z. F. Physik 77, 157-165.

Table 1: Definition of Symbols

Symbol	Units	Definition
$B(n)$	counts	Background counts for channel n
e	coulombs	Electronic charge
$E(\lambda)$		Overall counting efficiency for photons of wavelength λ
$E_\ell^+(\varepsilon_{i\ell})$		Positive ion collection efficiency for line emitting gas at electron energy $\varepsilon_{i\ell}$
$E_c^+(\varepsilon_{ic})$		Ditto for continuum emitting gas
$F_s(\lambda-\lambda_o)$		Normalized slit function of monochromator $F_s(0) = 1$
I_e	amps	Transmitted electron current
$I_\ell^+(\varepsilon_{i\ell})$	amps	Measured ion current in the line emitting gas, at electron energy $\varepsilon_{i\ell}$
$I_c^+(\varepsilon_{ic})$	amps	Ditto for continuum emitting gas
L	cm	Length of interaction region of crossed beams
N	cm^{-3}	Average neutral density in interaction region
$N_c(n)$	counts	Photon counts accumulated in channel n of MCS
$\dot{N}_\ell(\lambda_\ell,\varepsilon_\ell)$	counts-s^{-1}	Photon count rate when tuned to line emission at λ_ℓ at electron energy ε_ℓ
$\dot{N}_c(\lambda_o,\varepsilon_c)$	counts-s^{-1}	Photon count rate from continum measured at monochromator setting λ_o at electron energy ε_c
R^+		Relative ion collection efficiency $= E_c^+(\varepsilon_{ic})/E_\ell^+(\varepsilon_{i\ell})$
$R(\lambda)$		Relative quantum efficiency [$= E(\lambda)/E(\text{ref})$]

Table 1: Definition of Symbols (Cont'd.)

Symbol	Units	Definition
S	$nm\text{-}s^{-1}$	Monochromator sweep speed
W_s	nm	Effective width of normalized slit function
W_{sc}	nm	Value of W_s for continuum measurements
W_{ch}	nm/ch.	Effective channel width of MCS for wavelength scans
ε	eV	Electron energy
λ	nm	Wavelength
λ_ℓ	nm	Wavelength of line emission
λ_o	nm	Wavelength setting of monochromator
$\sigma_\ell(\lambda_\ell,\varepsilon_\ell)$	cm^2	Total emission cross section for line centered at λ_ℓ, for electrons of energy ε_ℓ
$\sigma_{i\ell}(\varepsilon_{i\ell})$	cm^2	Total ionization cross section for line emitting gas at electron energy $\varepsilon_{i\ell}$
$\sigma_c(\lambda,\varepsilon_c)$	cm^2/nm	Continum emission cross section at wavelength λ for electrons of energy ε_c
$\sigma_c(\varepsilon_c)$	cm^2	Total continum emission cross section at electron energy ε_c
$\sigma_{ic}(\varepsilon_{ic})$	cm^2	Total ionization cross section for continum emitting gas at electron energy ε_{ic}

Table 2. Photon Couhting Configurations and Measured Instrument Function Effective Widths, W_s.

Configuration	A	B	C	C'
PM Tube	C 31024(a)	C 31024(a)	8575(b)	8575(b)
Grating	Lo Blaze 2360 g/mm	Hi Blaze 1180 g/mm	Hi Blaze 1180 g/mm	Hi Blaze 1180 g/mm
Slits 500μ	0.835 nm	1.73 nm	1.73 nm	1.80 nm (c)
Size 1000μ	1.65 nm	3.43 nm	3.43 nm	

a) Operated at - 30°C, 2.4 kV

b) Operated at - 30°C, 1.5 kV

c) Measured prior to grating realignment

Table 3: Helium Ionization ($\sigma_{i\ell}$) and Line Emission (σ_{ℓ}) Cross Section

Reference Data from Literature

	a	b		
ε_{ℓ} eV	$\sigma_{i\ell}(\varepsilon_{\ell})$ (-16) cm^2	$\sigma_{\ell}(504.8,\varepsilon_{\ell})$ (-20) cm^2	$\sigma_{\ell}(443.8,\varepsilon_{\ell})$ (-20) cm^2	$\sigma_{\ell}(416.9,\varepsilon_{\ell})$ (-20) cm^2
35	0.125	(9.45) c	(3.85) c	(1.66) c
50	0.243	8.08	3.09	1.46
100	0.366	5.61	2.30	0.97
150	0.369	4.60 d	1.90 d	0.77 d

a) Rapp & Englander-Golden (1965)

b) Van Zyl et al. (1980)

c) Derived from previous measurements (Chantry & Chen, 1982)

d) Interpolated from 100 eV and 500 eV data points

Table 4. Examples of Helium Line Radiation Calibration Measurements

λ_ℓ nm	ε_ℓ eV	$\frac{\sigma_\ell(\lambda_\ell,\varepsilon_\ell)}{\sigma_{1\ell}(\varepsilon_\ell)}$	p (Bar.) torr	$I^+_\ell(\varepsilon_\ell)$ (-9) A	$\dot{N}_\ell(\lambda_\ell,\varepsilon_\ell)$ $-B_\ell$, sec^{-1}	$\frac{I^+_\ell}{\dot{N}_\ell}$	$\frac{\sigma_\ell}{\sigma_{1\ell}}\frac{I^+_\ell}{\dot{N}_\ell}R(\lambda_\ell)$
416.9[(a)]	35	1.33(-3)	0.668	1.53	171	0.895(-11)	2.02(-14)
$R(\lambda_\ell)$ = 1.7			0.984	2.40	277	0.866(-11)	1.96(-14)
	50 6.01(-4)	0.665	3.0	154	1.948(-11)	1.99(-14)	
		0.982	4.6	235	1.957(-11)	2.00(-14)	
	100 2.65(-4)	0.664	4.75	126	3.77(-11)	1.70(-14)	
		0.980	7.4	188	3.94(-11)	1.78(-14)	
	150 2.09(-4)	0.658	5.35	110	4.86(-11)	1.73(-14)	
		0.978	7.85	256	5.03(-11)	1.79(-14)	
443.8[(a)]	35	3.08(-3)	0.601	1.38	304	0.454(-11)	2.19(-14)
$R(\lambda_\ell)$ = 1.57			0.656	1.53	328	0.466(-11)	2.25(-14)
		0.962	2.35	497	0.473(-11)	2.29(-14)	
	50 1.27(-3)	0.600	2.76	263	1.049(-11)	2.09(-14)	
		0.654	2.90	276	1.051(-11)	2.10(-14)	
		0.959	4.50	436	1.032(-11)	2.06(-14)	
	100 6.28(-4)	0.599	4.30	209	2.057((11)	2.03(-14)	
		0.653	4.70	229	2.052(-11)	2.02(-14)	
		0.958	7.2	358	2.011(-11)	1.98(-14)	
	150 5.15(-4)	0.598	4.80	182	2.637(-11)	2.13(-14)	
		0.956	7.70	288	2.673(-11)	2.16(-14)	
504.8[(a)]	35	7.56(-3)	0.561	1.24	451	0.275(-11)	2.45(-14)
$R(\lambda_\ell)$ = 1.18			0.974	2.40	834	0.288(-11)	2.57(-14)
	50 3.33(-3)	0.56	2.52	398	0.633(-11)	2.49(-14)	
		0.972	4.60	723	0.636(-11)	2.50(-14)	
	100 1.53(-3)	0.56	3.90	314	1.242(-11)	2.24(-14)	
		0.971	7.30	585	1.248(-11)	2.25(-14)	
	150 1.25(-3)	0.558	4.45	282	1.578(-11)	2.33(-14)	
		0.970	7.70	487	1.581(-11)	2.33(-14)	

a) Using B500 optical configuration (see Table 2)

Table 5. Examples of Helium Line Radiation Calibration Measurements

λ_ℓ nm	ε_ℓ eV	$\dfrac{\sigma_\ell(\lambda_\ell,\varepsilon_\ell)}{\sigma_{i\ell}(\varepsilon_\ell)}$	p (Bar.) torr	$I^+_\ell(\varepsilon_\ell)$ (-9) A	$\dot{N}_\ell(\lambda_\ell,\varepsilon_\ell)$ $-B_\ell$, $\sec^{-1}$	$\dfrac{I^+_\ell}{\dot{N}_\ell}$	$\dfrac{I^+_\ell}{\sigma_{i\ell}}\,\dfrac{I^+_\ell}{\dot{N}_\ell}\,R(\lambda_\ell)$
416.9(a)	35	1.35(-3)	0.871	2.1	226	0.929(-11)	2.10(-14)
$R(\lambda_\ell)$ = 1.7	50	6.01(-4)	0.869	4.0	197	2.03(-11)	2.07(-14)
100	2.65(-4)	0.867	6.4	153	4.18(-11)	1.88(-14)	
150	2.09(-4)	0.865	6.75	128	5.27(-11)	1.87(-14)	
416.9(b)	35	1.33(-3)	0.447	0.96	238	0.403(-11)	2.00(-14)
$R(\lambda_\ell)$ = 3.74	50	6.01(-4)	0.446	1.9	210	0.905(-11)	2.03(-14)
100	2.65(-4)	0.445	3.0	165	1.82(-11)	1.80(-14)	
150	2.09(-4)	0.444	3.2	130	2.46(-11)	1.92(-14)	
443.8(a)	35	3.08(-3)	0.841	2.02	359	0.563(-11)	2.22(-14)
$R(\lambda_\ell)$ = 1.28	50	1.27(-3)	0.838	3.85	311	1.238(-11)	2.01(-14)
100	6.28(-4)	0.837	6.15	246	2.50(-11)	2.01(-14)	
150	5.15(-4)	0.835	6.45	202	3.19(-11)	2.10(-14)	
443.8(b)	35	3.08(-3)	0.435	0.93	391	0.238(-11)	2.06(-14)
$R(\lambda_\ell)$ = 2.82			0.747	1.65	672	0.245(-11)	2.12(-14)
50	1.27(-3)	0.434	1.82	342	0.532(-11)	1.90(-14)	
		0.746	3.20	591	0.541(-11)	1.93(-14)	
100	6.28([illegible])	0.433	3.0	275	1.09(-11)	1.93(14)	
		0.744	5.2	460	1.13(-11)	2.00(-14)	
150	5.15(-4)	0.432	3.05	230	1.326(-11)	1.92(-14)	
		0.743	5.45	384	1.419(-11)	2.06(-14)	

a) Using A500 optical configuration (see Table 2)
b) Using A1000 optical configuration (see Table 2)

FIGURE CAPTIONS

Figure 1	Schematic of crossed beam system
Figure 2	Schematic diagram of the optical system, shown approximately to scale. $L_{1,2}$ are quartz lenses. $S_{1,2}$ are the entrance and exit slits of the Jarrell-Ash 0.25 meter Ebert monochromator. Two light baffles (out of five) are shown. They serve to reduce the scattered light from the electron gun filament entering the optical system.
Figure 3	Relative Photon Counting Efficiencies of the various optical configurations. For the present series of measurements configuration A was mostly used. All curves were measured with 500μ slits. Use of 1000μ slits raises the curves by a factor of 2.20.
Figure 4	An example of the instrumental line shape measured by scanning the He emission lines shown. These particular measurements are for optical configuration A1000, i.e., using the grating having 2360 g/mm, and 1000μm slits. The multichannel scaler was scanned at 0.2 nm channel. Applying Equation (21) to this data gives W_s = 1.65 nm, listed in Table 2.
Figure 5	Examples of raw data photon counts as a function of wavelength ε at electron energies ε = 8 and 35 eV using W_{ch} = 0.5 nm. The various mercury lines indicated are used for wavelength calibration.
Figure 6	Wavelength resolved emission cross sections of $HgBr_2$ measured at the indicated electron energies. The curves shown are obtained from data of the type displayed in Figure 5 by (i) removing the Hg line contributions at the positions marked, (ii) correcting for the relative quantum detection efficiency, and (iii) using He line measurements for calibration. The vertical bars above the 35 eV curve indicate the positions listed by Wieland (1932) for maxima in the fluorescence.

Figure 7 Showing the dependence on $HgBr_2$ beam density of the fluorescence signals at the indicated wavelengths. The positive ion signal is used as a measure of the beam density, which is controlled by the reservoir temperature.

Figure 8 Illustrating the procedure adopted for partitioning the fluorescence spectra into the relevant bands. The B-X band is assumed to decrease linearly to zero between 441.5 nm and 295.5 nm. Thus, at this electron energy (7.5 eV), most of the signal in this range is assigned to the (B-X) band. Compare with Figure 9.

Figure 9 Data of the same type as Figure 8, but for an electron energy of 8 eV. Note the substantial increase in the signal assigned to the (B'-X) band.

Figure 10 Total emission cross sections for the bands indicated. The filled points are obtained from data of the type illustrated in Figures 5, 6, 8 and 9 using Equation (19) and (20). The curves shown below 30 eV were obtained by setting the monochromator at the peak wavelength for each band, and scanning the electron energy synchronously with the multichannel scaler, with the resulting curves scaled to match the filled points in the plateau regions. The open points between 30 and 150 eV were obtained similarly, with the broken curves indicating a reasonable smooth interpolation between the points. Independently measured thresholds for the three curves are σ_c(B'-X): 7.45 eV: σ_c(C-X):7.40 eV; and σ_c(D-X):7.65 eV.

Figure 11 Showing the same data as Figure 10, plus data on the emission cross section for the (B-X) band of $HgBr^*$. The full curve labelled σ_c(B-X) is obtained by reanalyzing our previous data by the procedure developed from the present series of measurements. The filled points are from the present measurements. The curve labelled $\Sigma\sigma_c$(D,C,B'-X) is the sum of the three lower curves.

Figure 12 Trapped electron and positive ion signals measured in $HgBr_2$. The electron energy scale is given by the extrapolated threshold for the positive ion signal, at 10.60 eV. The broken curve labelled I^- is an estimate of the negative ion contribution to the total negative signal, labelled I^e. Arrows labelled A-D indicate inferred inelastic loss thresholds, at 5.1, 6.0, 7.4, and 9.15 eV respectively.

Figure 13 Wavelength resolved emission cross sections measured previously at the indicated electron energies (Chantry & Chen, 1982), but with a revised calibration based on the present series of He line measurements.

Dwg. 7739A23

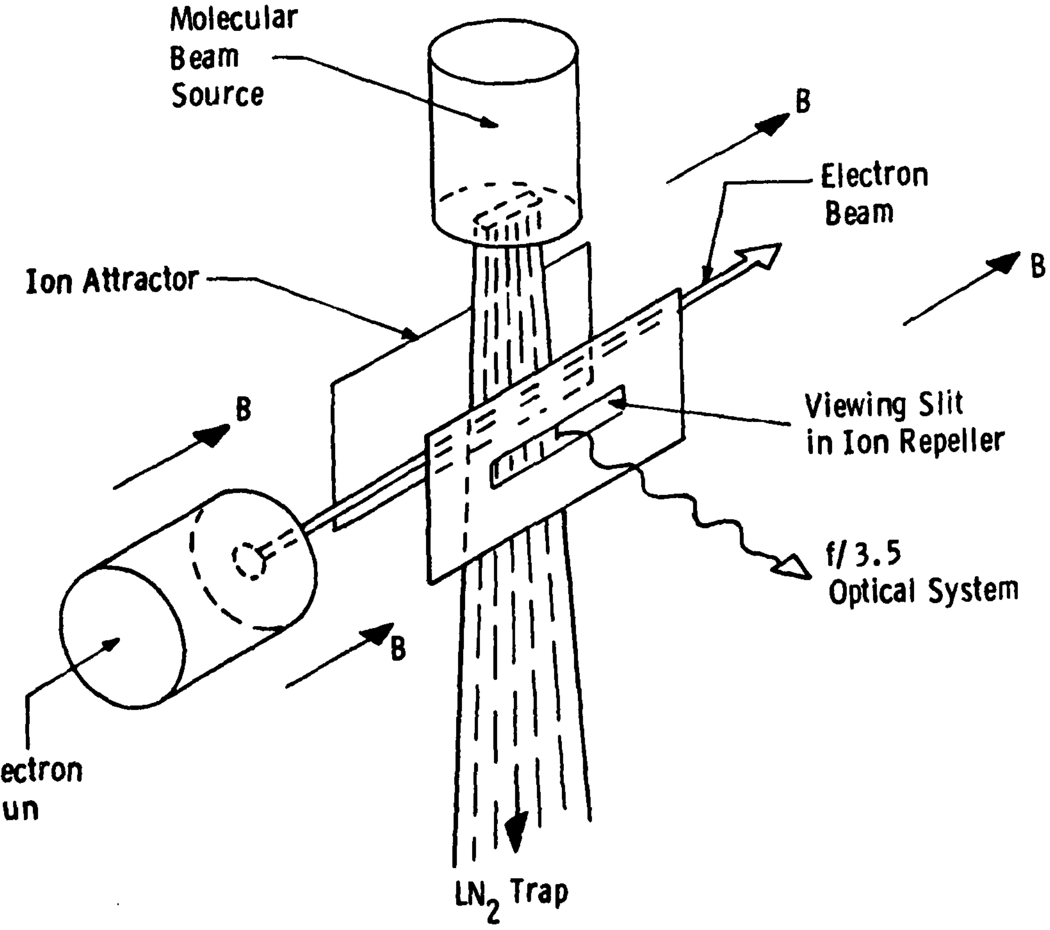

Fig. 1 Schematic of crossed beam system

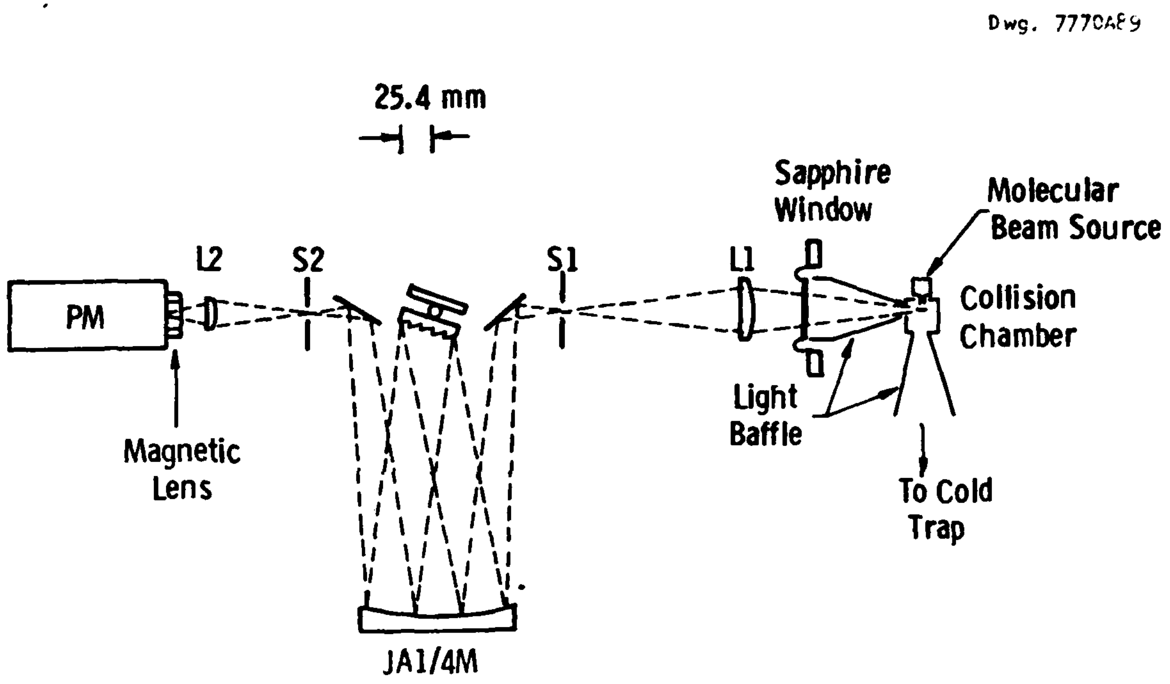

Figure 2. Schematic diagram of the optical system, shown approximately to scale. $L_{1,2}$ are quartz lenses. $S_{1,2}$ are the entrance and exit slits of the Jarrell-Ash 0.25 meter Ebert monochromator. Two light baffles (out of five) are shown. They serve to reduce the scattered light from the electron gun filament entering the optical system.

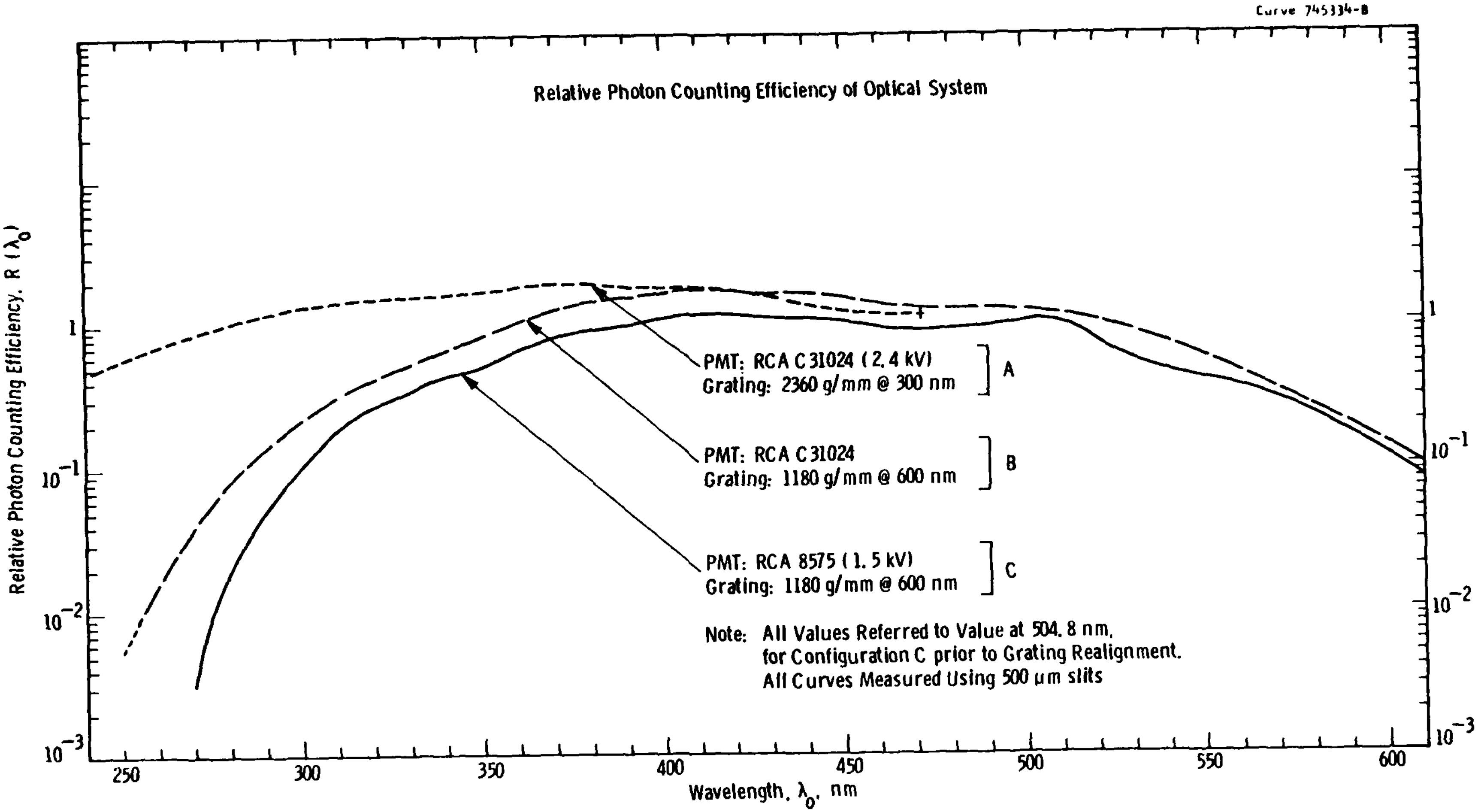

Figure 3. Relative Photon Counting Efficiencies of the various optical configurations. For the present series of measurements configuration A was mostly used. All curves were measured with 500μ slits. Use of 1000μ slits raises the curves by a factor of 2.20.

Curve 745329-B

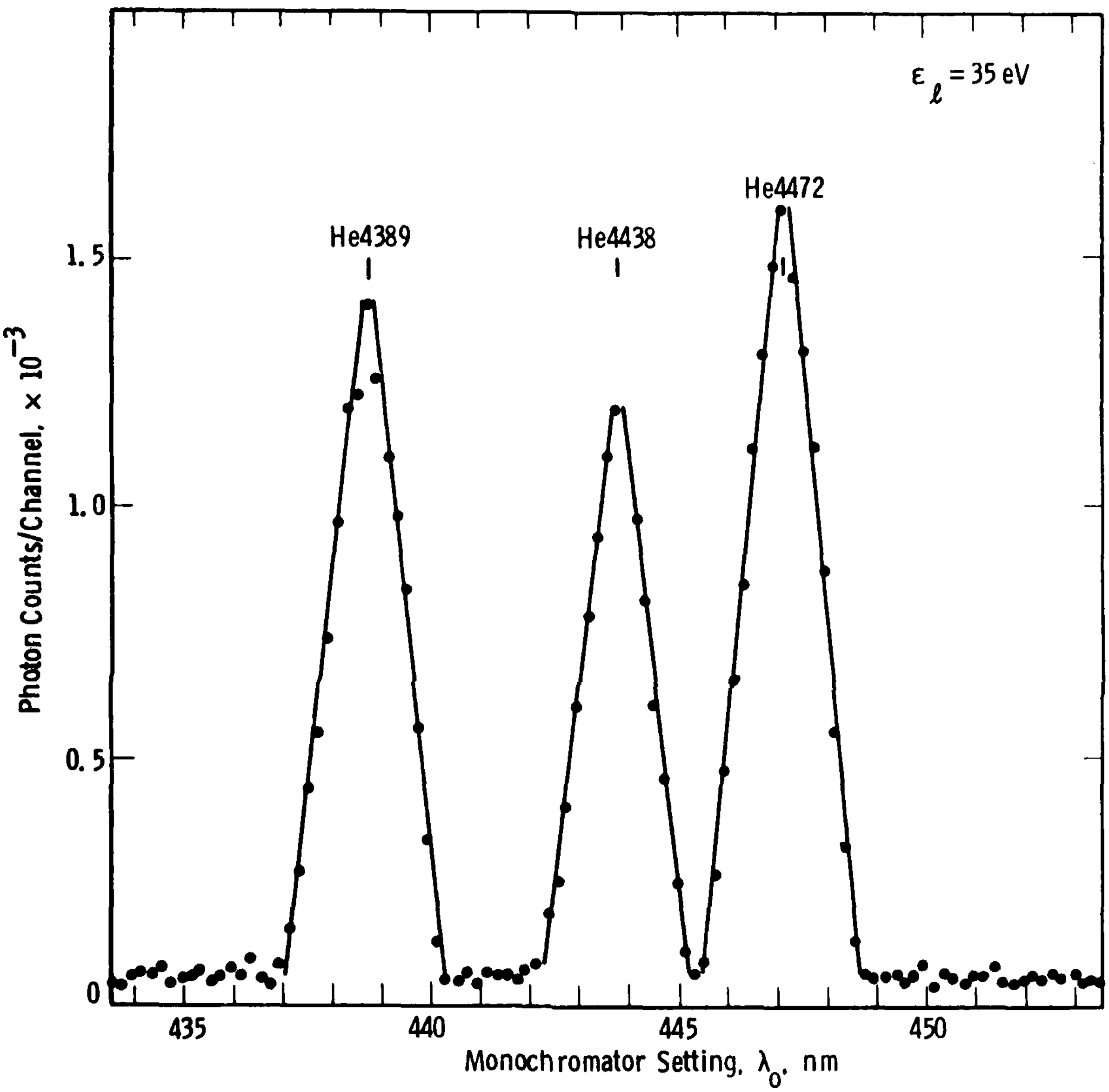

Figure 4. An example of the instrumental line shape measured by scanning the He emission lines shown. These particular measurements are for optical configuration A1000, i.e., using the grating having 2360 g/mm, and 1000μm slits. The multichannel scaler was scanned at 2A/channel. Applying Equation (21) to this data gives W_s = 1.65 nm, listed in Table 2.

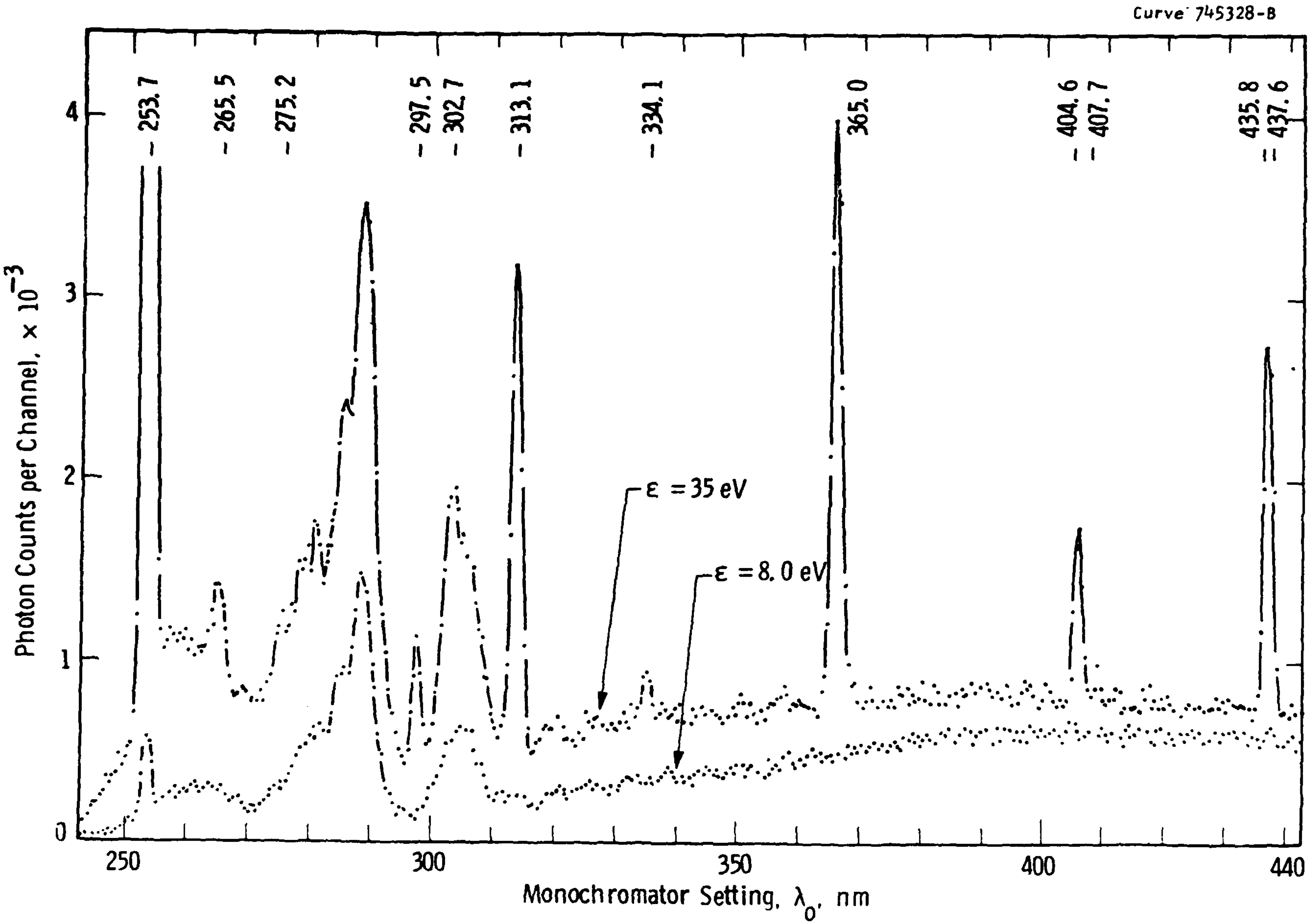

Figure 5. Examples of raw data photon counts as a function of wavelength ε at electron energies ε = 8 and 35 eV using W_{ch} = 5A. The various mercury lines indicated are used for wavelength calibration.

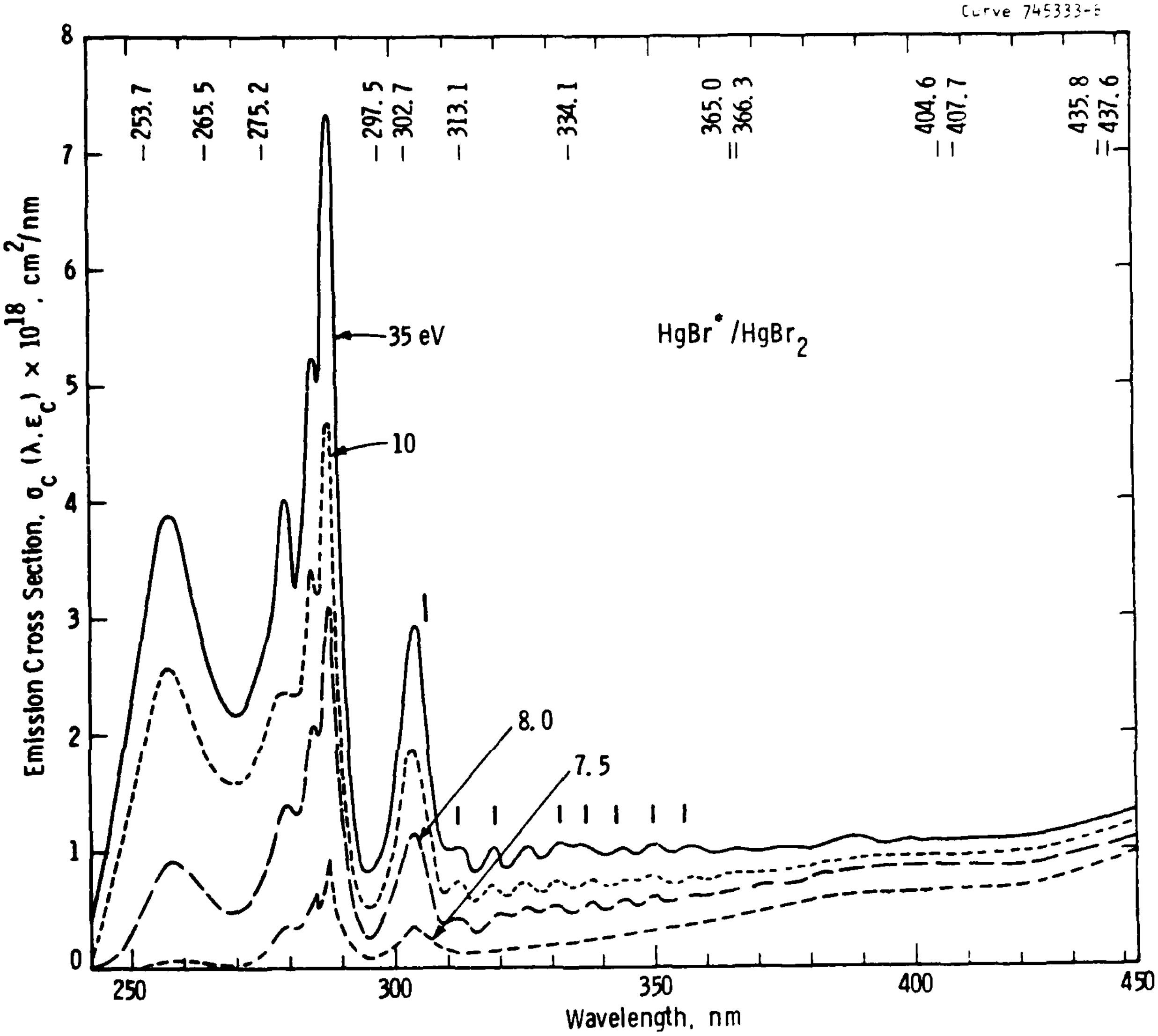

Figure 6. Wavelength resolved emission cross sections of $HgBr_2$ measured at the indicated electron energies. The curves shown are obtained from data of the type displayed in Figure 5 by (i) removing the Hg line contributions at the positions marked, (ii) correcting for the relative quantum detection efficiency, and (iii) using He line measurements for calibration. The vertical bars above the 35 eV curve indicate the positions listed by Wieland (1932) for maxima in the fluorescence.

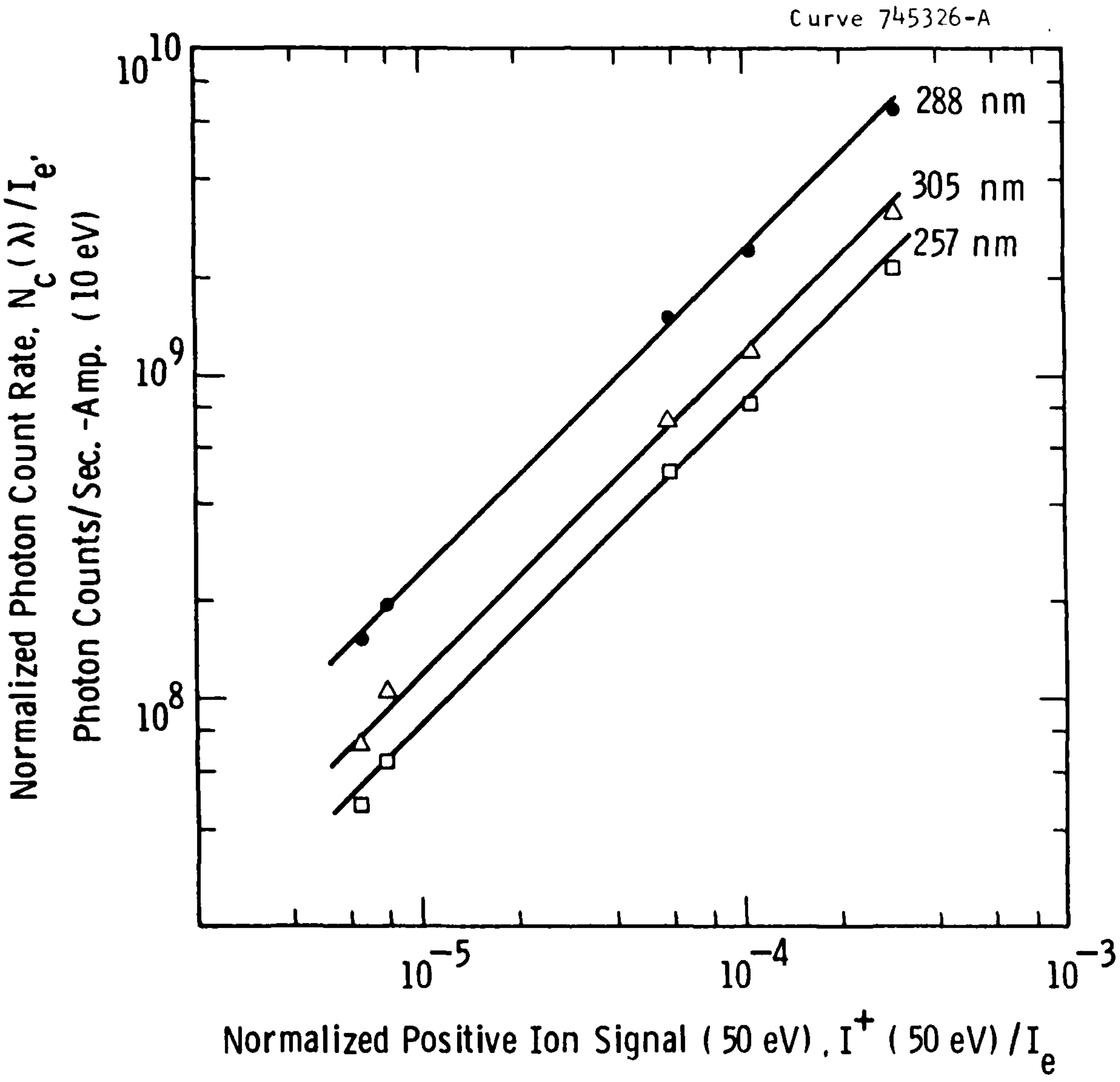

Figure 7. Showing the dependence on $HgBr_2$ beam density of the fluorescence signals at the indicated wavelengths. The positive ion signal is used as a measure of the beam density, which is controlled by the reservoir temperature.

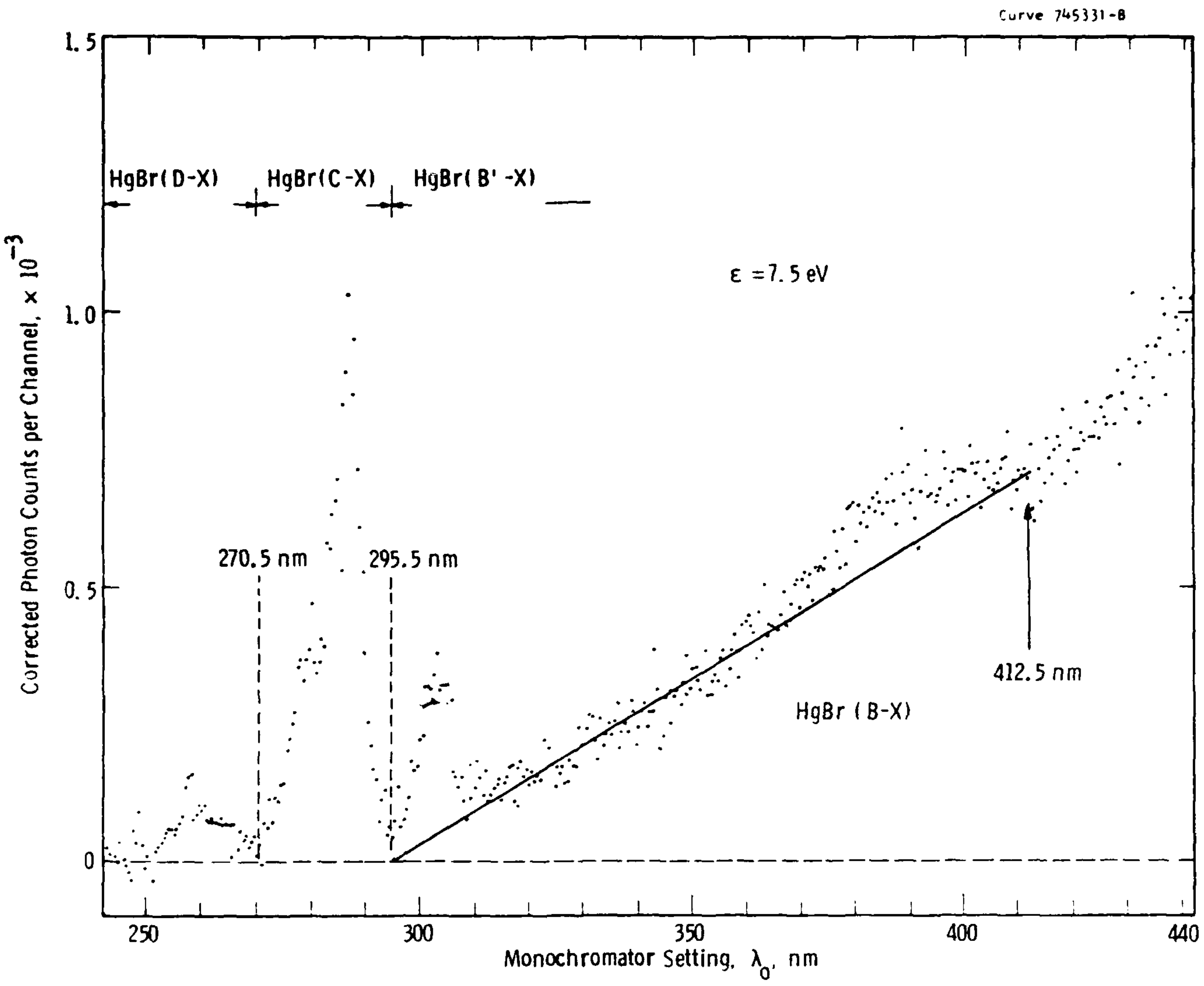

Figure 8. Illustrating the procedure adopted for partitioning the fluorescence spectra into the relevant bands. The B-X band is assumed to decrease linearly to zero between 441.5 nm and 295.5 nm. Thus, at this electron energy (7.5 eV), most of the signal in this range is assigned to the (B-X) band. Compare with Figure 9.

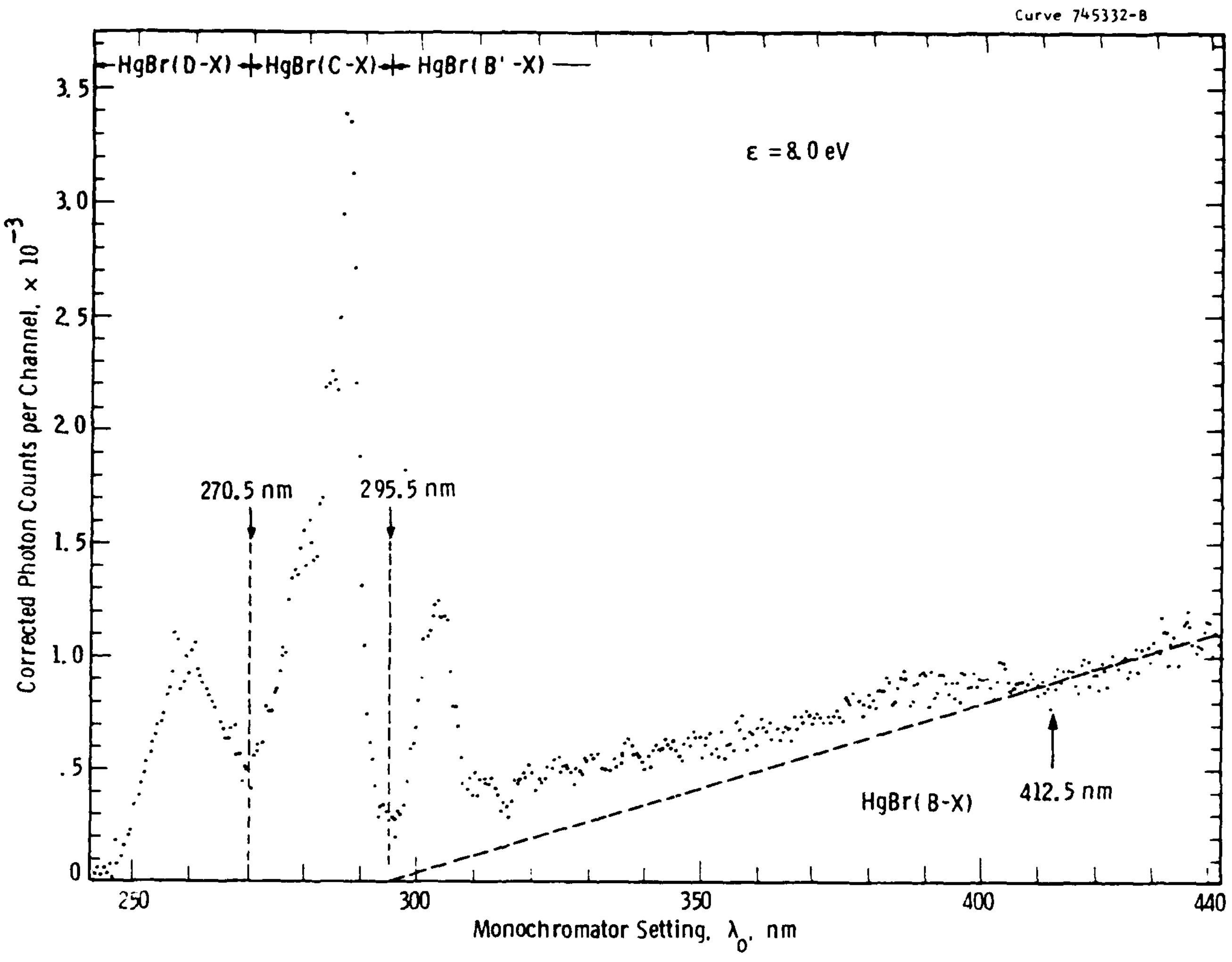

Figure 9. Data of the same type as Figure 8, but for an electron energy of 8 eV. Note the substantial increase in the signal assigned to the (B'-X) band.

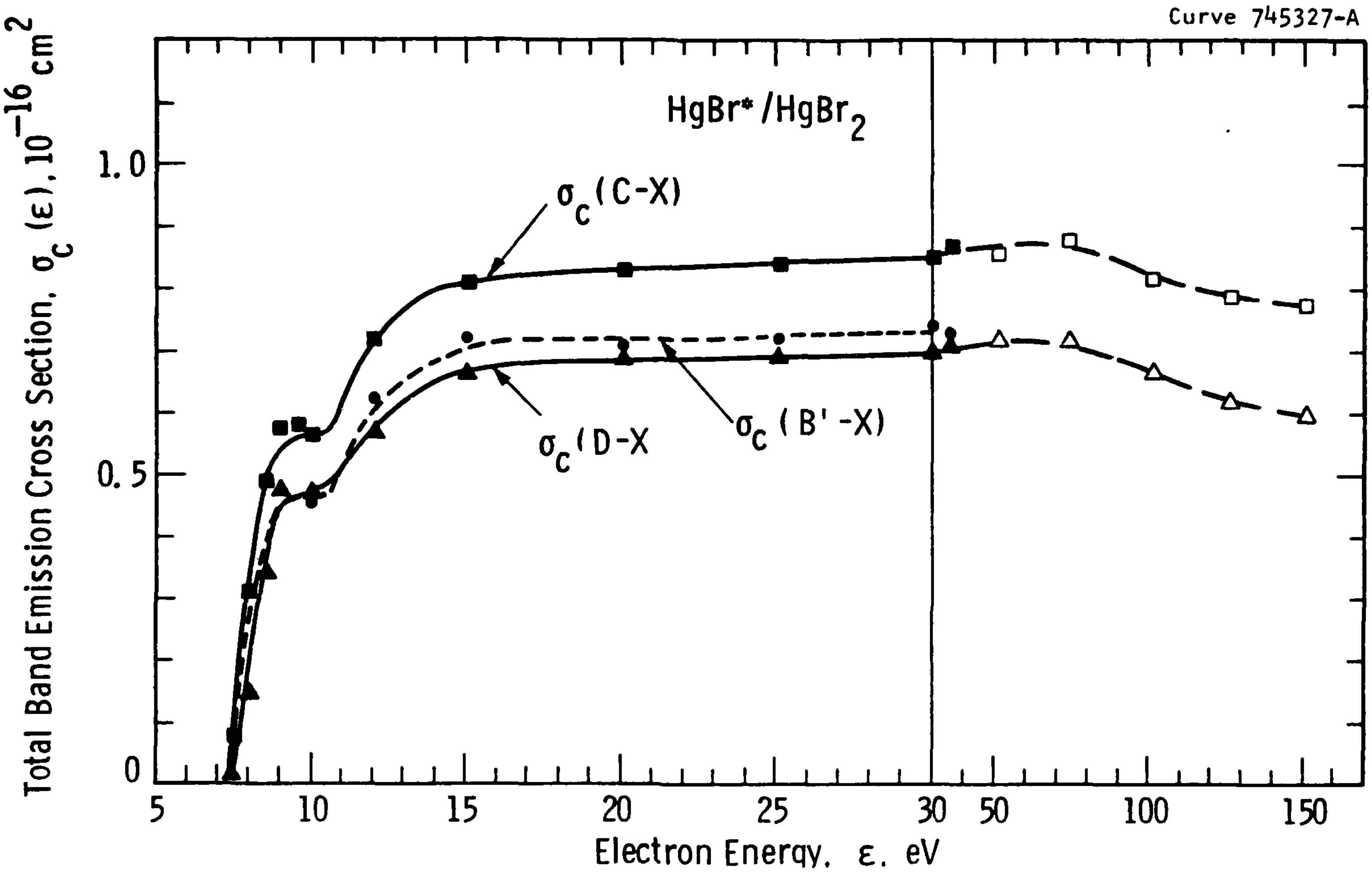

Figure 10. Total emission cross sections for the bands indicated. The filled points are obtained from data of the type illustrated in Figures 5, 6, 8 and 9 using Equation (19) and (20). The curves shown below 30 eV were obtained by setting the monochromator at the peak wavelength for each band, and scanning the electron energy synchronously with the multichannel scaler, with the resulting curves scaled to match the filled points in the plateau regions. The open points between 30 and 150 eV were obtained similarly, with the broken curves indicating a reasonable smooth interpolation between the points. Independently measured thresholds for the three curves are σ_c(B'-X):7.45 eV; σ_c(C-X):7.40 eV; and σ_c(D-X):7.65 eV.

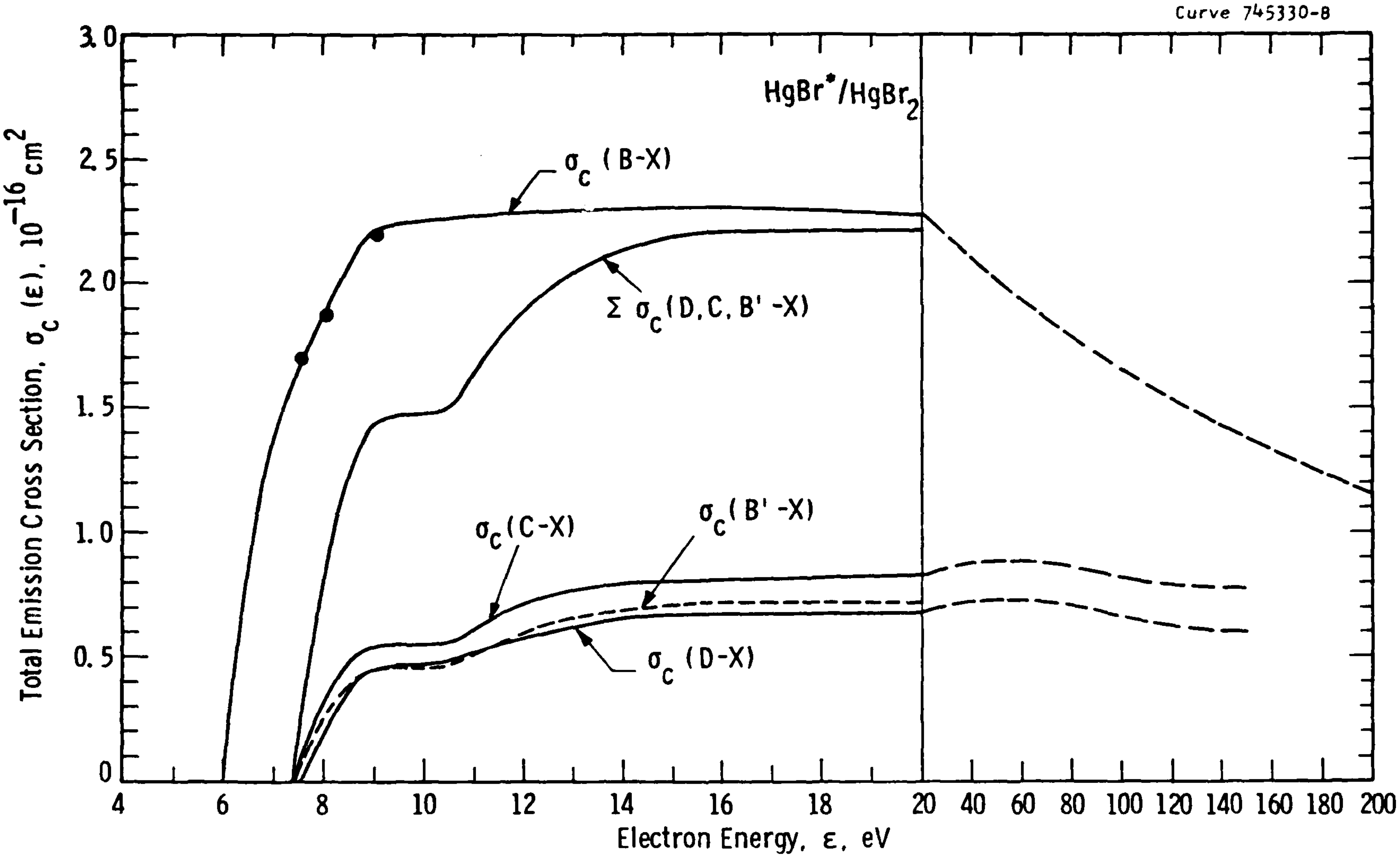

Figure 11. Showing the same data as Figure 10, plus data on the emission cross section for the (B-X) band of HgBr*. The full curve labelled σ_c(B-X) is obtained by reanalyzing our previous data by the procedure developed from the present series of measurements. The filled points are from the present measurements. The curve labelled $\Sigma\sigma_c$(D,C,B'-X) is the sum of the three lower curves.

Curve 745627-B

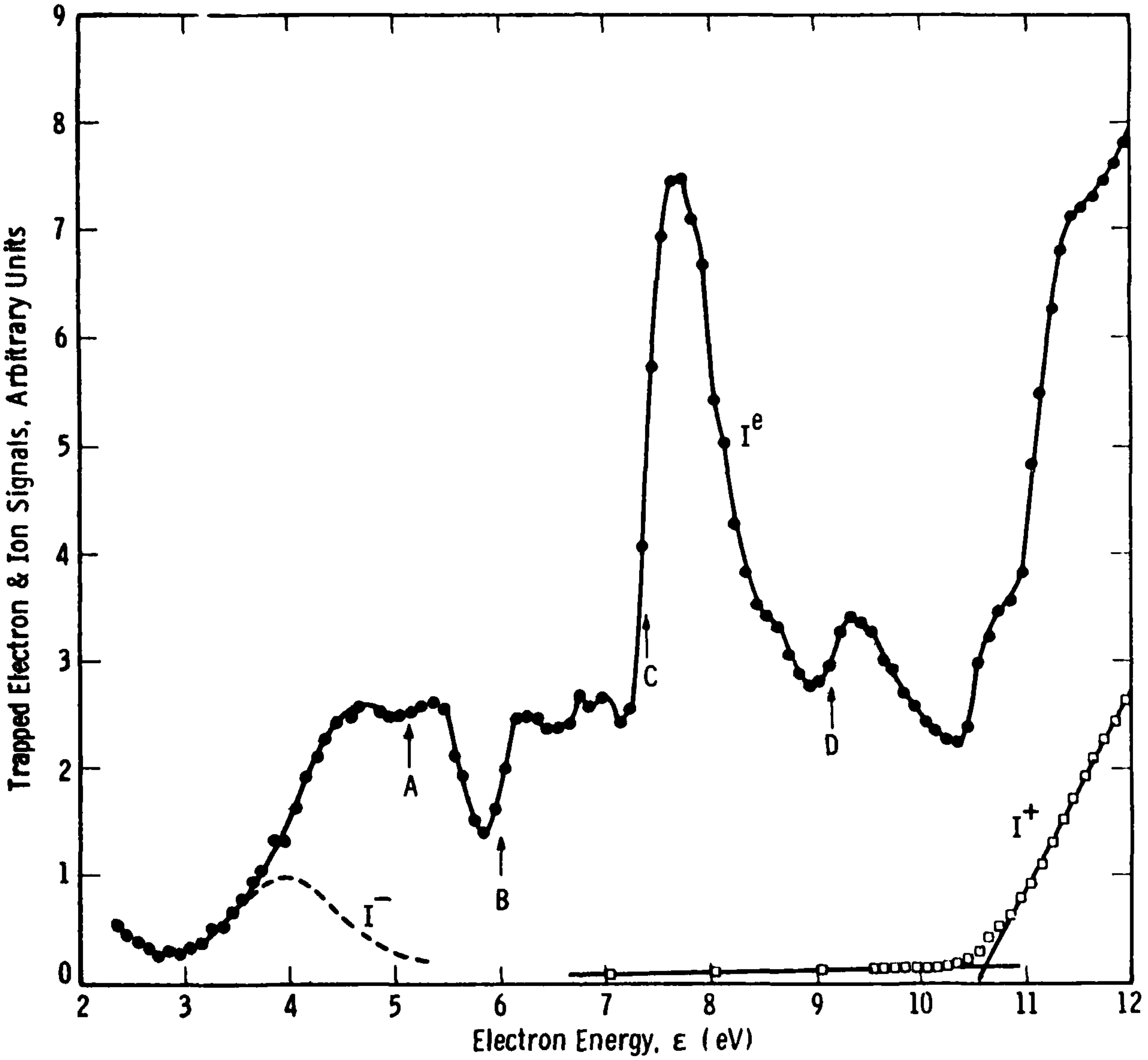

Figure 12. Trapped electron and positive ion signals measured in $HgBr_2$. The electron energy scale is given by the extrapolated threshold for the positive ion signal, at 10.60 eV. The broken curve labelled I^- is an estimate of the negative ion contribution to the total negative signal, labelled I^e. Arrows labelled A-D indicate inferred inelastic loss thresholds, at 5.1, 6.0, 7.4, and 9.15 eV respectively.

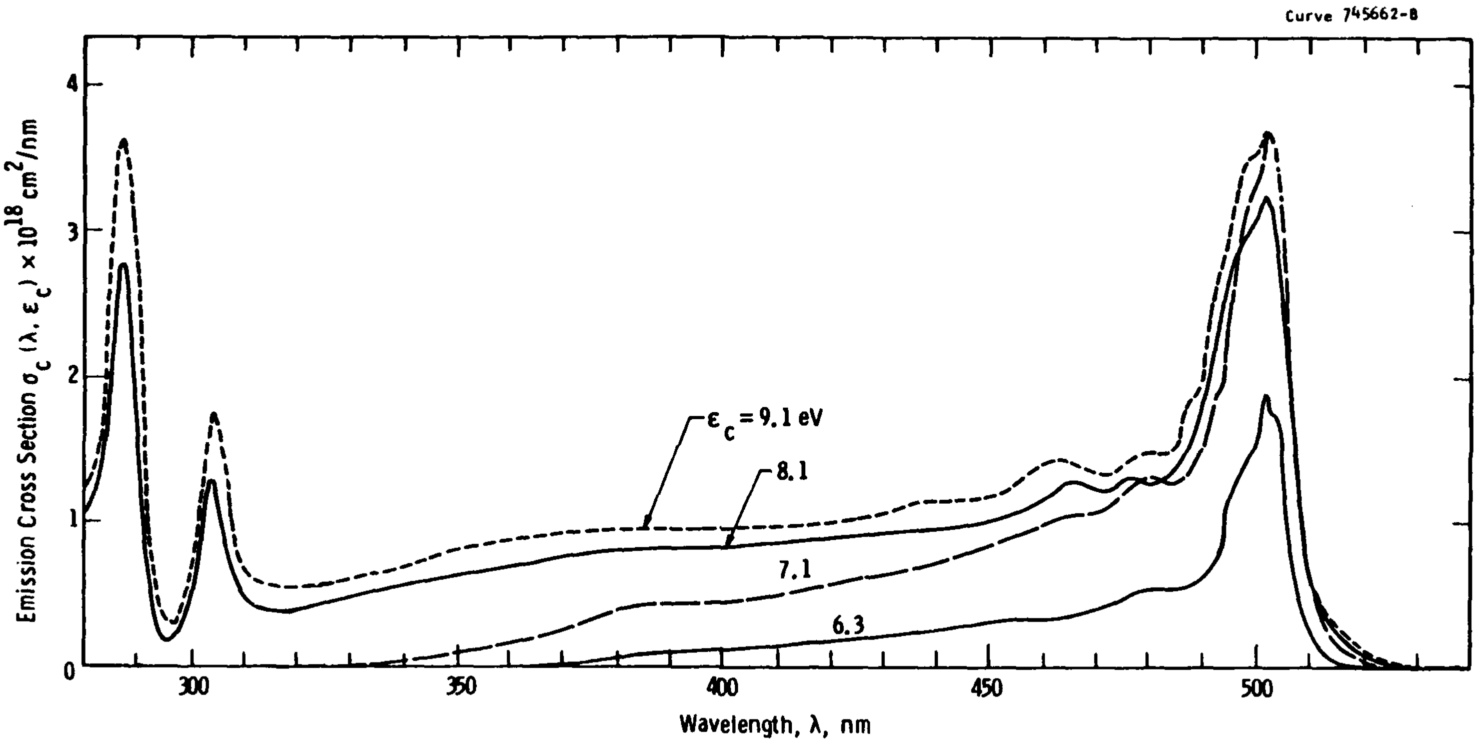

Figure 13. Wavelength resolved emission cross sections measured previously at the indicated electron energies (Chantry & Chen, 1982), but with a revised calibration based on the present series of He line measurements.

ILMED

02 – 84